

1 **Palaeo-environmental evolution of Central Asia during the Cenozoic: New insights from**
2 **the continental sedimentary archive of the Valley of Lakes (Mongolia)**

3

4 Andre Baldermann^{1*}, Oliver Wasser¹, Elshan Abdullayev^{2,3}, Stefano Bernasconi⁴, Stefan
5 Löhr⁵, Klaus Wemmer⁶, Werner E. Piller⁷, Maxim Rudmin⁸ and Sylvain Richoz⁹

6

7 ¹Institute of Applied Geosciences, Graz University of Technology, NAWI Graz Geocenter, Graz,
8 Austria; baldermann@tugraz.at; oliver.wasser@student.tugraz.at

9 ²Department of Life Sciences, Khazar University, Baku, Azerbaijan; elabdulla3@gmail.com

10 ³Department of Geoscience, French-Azerbaijani University (UFAZ), Baku, Azerbaijan;
11 elabdulla3@gmail.com

12 ⁴Geological Institute, ETH Zurich, Zurich, Switzerland; stefano.bernasconi@erdw.ethz.ch

13 ⁵Department of Earth and Environmental Sciences, Macquarie University, Sydney, Australia;
14 stefan.loehr@mq.edu.au

15 ⁶Geoscience Centre (GZG), University of Göttingen, Göttingen, Germany; kwemmer@gwdg.de

16 ⁷Institute of Earth Sciences, University of Graz, NAWI Graz Geocenter, Graz, Austria;
17 werner.piller@uni-graz.at

18 ⁸Division of Geology, Tomsk Polytechnic University, Tomsk, Russia; rudminma@tpu.ru

19 ⁹Department of Geology, University of Lund, Lund, Sweden; sylvain.richoz@geol.lu.se

20

21 *Corresponding author: Andre Baldermann

22 Institute of Applied Geosciences, Graz University of Technology, 8010, Graz, Austria

23 Tel: +43 316 873 6850, Fax: +43 316 873 6876; E-mail: baldermann@tugraz.at

24

25 Key Words: Cenozoic climate change; Central Asia; Palaeo-environment; Westerly winds;
26 Hydroclimate; Paleosols

27 **Abstract**

28 The Valley of Lakes basin (Mongolia) contains a unique continental sedimentary archive,
29 suitable for constraining the influence of tectonics and climate change on the aridification of
30 Central Asia in the Cenozoic. We identify the sedimentary provenance, the (post)depositional
31 environment and the palaeo-climate based on sedimentological, petrographical, mineralogical
32 and (isotope) geochemical signatures recorded in authigenic and detrital silicates as well as soil
33 carbonates in a sedimentary succession spanning ~34 to 21 Ma. The depositional setting was
34 characterized by an ephemeral braided river system draining prograding alluvial fans, with
35 episodes of lake, playa or open steppe sedimentation. Metamorphics from the northern adjacent
36 Neoproterozoic to late Proterozoic hinterlands provided a continuous influx of silicate detritus to
37 the basin, as indicated by K-Ar ages of detrital muscovite (~798-728 Ma) and discrimination
38 function analysis. The authigenic clay fraction is dominated by illite-smectite and “hairy” illite
39 (K-Ar ages: ~34-25 Ma), which formed during coupled petrogenesis and precipitation from
40 hydrothermal fluids originating from major basalt flow events (~32-29 Ma and ~29-25 Ma).
41 Changes in hydroclimate are recorded in $\delta^{18}\text{O}$ and $\delta^{13}\text{C}$ profiles of soil carbonates and in silicate
42 mineral weathering patterns, indicating comparatively humid to semi-arid conditions prevailed
43 in the late(st) Eocene, changing into arid conditions in the Oligocene and back to humid to
44 semi-arid conditions in the early Miocene. Aridification steps are indicated at ~34-33 Ma, ~31
45 Ma, ~28 Ma and ~23 Ma and coincide with some episodes of high-latitude ice sheet expansion
46 inferred from marine deep-sea sedimentary records. This suggests long-term variations of the
47 ocean/atmosphere circulation patterns due to $p\text{CO}_2$ fall, re-configurations of ocean gateways
48 and ice-sheet expansion in Antarctica could have impacted the hydroclimate and weathering
49 regime in the basin. We conclude that the aridification in Central Asia was triggered by reduced
50 moisture influx by westerly winds driven by Cenozoic climate forcing and the exhumation of
51 the Tian Shan and Altai mountains and modulate by global climate events.

52 **1. Introduction**

53 The Cenozoic Era (66 Ma to the present day) saw several dramatic changes of the marine and
54 continental ecosystems (e.g., evolution of large plankton feeders such as baleen whales, shift
55 towards cold-water, high nutrient plankton assemblages at high latitude, expansion of terrestrial
56 mammals) major tectonic events (e.g., opening of Southern Hemisphere Oceanic gateways,
57 shift to the 4-layer structure of the modern ocean, collision of the African-Arabian-Eurasian
58 plates, uplift of the Alpine and Himalayan mountain belt) and global climate forcing (e.g.,
59 change from greenhouse to icehouse conditions) (Cerling, 1997; Houben et al., 2013; Norris et
60 al., 2013; Cermeño et al., 2015; Mutz et al., 2018; Komar and Zeebe, 2021). The acceleration
61 of Cenozoic climate cooling started after the Early Eocene Climatic Optimum (EECO; ~52-50
62 Ma), with temperatures ~10-12 °C warmer than the modern deep ocean, followed by the
63 appearance and expansion of the Antarctic ice-sheets after the Eocene-Oligocene Transition
64 (EOT; ~34 Ma) and ultimately culminating in the extensive Northern Hemisphere glaciation
65 of the Pleistocene (~2.6-0.01 Ma; Zachos et al., 2001; Lear et al., 2008; Mudelsee et al., 2014;
66 Abdullayev et al., 2021). This long-term transition in Earth`s climate is well documented in
67 marine sedimentary archives, but its impact on the evolution of continental ecosystems remains
68 poorly constrained, mainly because continuous, well preserved terrestrial records are scarce
69 and the responses to climate change in these settings are highly complex, depending on latitude,
70 proximity to coast and mountain ranges, position relative to climatic winds, vegetation etc.
71 (e.g., Caves Rügenstein and Chamberlain, 2018; Baldermann et al., 2020). An exception is the
72 sedimentary archive of the Valley of Lakes (Mongolia), which hosts a ~34-21 Ma record of
73 continental sedimentation in Central Asia. The biostratigraphy and the correlation between
74 different outcrops in this basin are well established based on mammalian communities and
75 gastropod records (Harzhauser et al., 2017), magnetostratigraphy (Sun and Windley, 2015) and
76 radiometric age dating of different basalt horizons (Daxner-Höck et al., 2017), rendering this

77 locality suitable for constraining the links between tectonism and climate change in Central
78 Asia during the Cenozoic. The Eocene to Miocene of Central Asia was characterized by
79 accelerated aridification (Dupont-Nivet et al., 2007; Xiao et al., 2010; Bosboom et al., 2014;
80 Li et al., 2016), expressed as a substantially expanded Gobi Desert relative to today (Guo et
81 al., 2008; Lu et al., 2019) and a sudden turnover in the mammal record (Harzhauser et al., 2016;
82 Barbolini et al., 2020). Several, partially opposing hypotheses have been proposed to explain
83 the aridification of Central Asia, including a combination of orbitally-driven climate forcing,
84 the stepwise retreat of the proto-Paratethys Sea and uplift of the Tibetan Plateau (Pälike et al.,
85 2006; [Zhang et al., 2013](#); Li et al., 2020) or a continuous decrease of moisture transport by the
86 westerlies due to exhumation of the Tian Shan and Altai mountains (Caves et al., 2014; Caves
87 et al., 2015; Caves Rügenstein and Chamberlain, 2018). However, the evolution of Central
88 Asia's hydroclimate in the Cenozoic was not a period of continuous aridification; indeed, the
89 climatic conditions in particular in the Oligocene were highly complex and characterized by
90 numerous glacial-interglacial cycles (Xiao et al., 2010). Recently, Richoz et al. (2017) have
91 identified two aridification pulses in Central Asia, in the early and late Oligocene, which they
92 assigned to global climatic events. To date, a correlation of the global marine record with the
93 terrestrial record of Mongolia is barely developed (Harzhauser et al., 2016; Harzhauser et al.,
94 2017; Richoz et al., 2017), which limits our understanding of the relative influences of climate
95 change and regional tectonics on the evolution of hydroclimate and weathering conditions in
96 Central Asia in the Cenozoic.

97 In this contribution, we greatly extend the existing mineralogical and (isotope) geochemical
98 dataset previously reported in Richoz et al. (2017) for the Eocene-Miocene sediments from the
99 Valley of Lakes (Mongolia): K-Ar ages and polytype analysis of detrital and authigenic illitic
100 phases coupled with discrimination function analysis and sedimentological-petrographical-
101 geochemical inspection are used to constrain provenance, palaeo-environmental conditions and

102 post-depositional alteration history of this sedimentary succession. Systematic, coherent
103 changes in the weathering patterns of silicate detritus and pristine $\delta^{18}\text{O}$ and $\delta^{13}\text{C}$ signatures
104 recorded in paleosols carbonates allow us to revise and refine the evolution of hydroclimate
105 and weathering conditions in Central Asia in the Cenozoic.

106

107 **2. Geological framework**

108 The Valley of Lakes is an ESE-WNW striking sedimentary basin with ~500 km extension in
109 largest dimension. It is located in Central Mongolia and bordered by the Khangai mountains in
110 the north and the Gobi Altai mountains in the south (Fig. 1a). The geological super-units in the
111 north of Mongolia contain Neoproterozoic, Proterozoic and Palaeozoic rocks of the Caledonian
112 orogen as well as late Neoproterozoic to Ordovician (Tuva-Mongol) magmatic arc and related
113 back- and fore-arc intrusions, accretionary wedge sequences and ophiolites (Porter, 2016). The
114 geological super-units in the south are characterized mainly by a Palaeozoic orogen, especially
115 the Kazakh-Mongol magmatic arc, which forms the border between Mongolia and China.
116 These units include mainly Devonian to Carboniferous island arc volcanic rocks, Ordovician
117 to Silurian volcanics, Ordovician to Carboniferous metamorphosed sedimentary sequences and
118 Permo-Carboniferous granitoids (Porter, 2016).

119 Regarding the regional lithostratigraphic context, the northern structural units of the Valley of
120 Lakes basin in the Taastsiin Gol area comprise dominantly fault- and thrust-bounded crystalline
121 basement of Neoproterozoic to Palaeozoic age (Fig. 1b). These include the Baidrag (high-grade
122 gneisses, charnockites and amphibolites, up to 2.65 Ga old) and the Burdgal zone (metapelites,
123 metapsammities and metacherts, 699 ± 35 Ma) in its southernmost end (Teraoka et al., 1996).
124 Further structural units towards the north are the Bayan Khongor (metamorphosed basic rocks,
125 ophiolites and pelitic schists, 450 Ma), the Dzag (metapelites and metapsammities, 440 ± 22
126 Ma and 395 ± 20 Ma) and the Khangai zone (unmetamorphosed, but tectonically deformed

127 sandstones, mudstones and intercalated olistolith sequences of unspecified Devonian to
128 Carboniferous age) (Teraoka et al., 1996; Höck et al., 1999). All of these zones are intruded by
129 numerous granitoids of variable age (Proterozoic to Cretaceous) and composition (Höck et al.,
130 1999). The major zones located in the south of the Valley of Lakes basin comprise the Baga
131 Bogd, the Ikh Bogd and the Bogd som, which are petrographically indistinguishable from the
132 time-equivalent metasediments and metavolcanics of the Bayan Khongor zone and of the
133 Permian quartzitic conglomerates from the adjacent Mount Ushgoeg (Höck et al., 1999).

134 In the focus of this study are the fossiliferous siliciclastic sediments of the Taatsiin Gol Basin,
135 which record important information about changes in sediment provenance, weathering paths
136 and conditions and palaeo-climate in Central Asia during the Eocene to Miocene. The herein
137 investigated sedimentary sections span the Tsagaan Ovoo Formation (upper Eocene), the
138 Hsanda Gol Formation (Oligocene) and the Loh Formation (lower Miocene). Five sections,
139 namely Taatsiin Gol right (TGR-AB), Taatsiin Gol south (TGR-C), Hsanda Gol (SHG-D),
140 Tatal Gol (TAT-E) and Hotuliin Teeg (HTE), were chosen for this study, because of the well-
141 constrained chronological framework at these localities. Based on previous radiometric and
142 magnetostratigraphic dating of these sections (Höck et al., 1999; Sun and Windley, 2015),
143 Harzhauser et al. (2017) have established a precise biozonation of the studied sedimentary
144 succession, which includes, from the bottom to the top, Zone A (early Rupelian: 33.9 Ma to
145 ~31.5 Ma), Zone B (late Rupelian: ~31.5 Ma to ~28.1 Ma), Zone C (early Chattian: ~28.1
146 Ma to ~25.6 Ma), Zone C1 (mid-Chattian: ~25.6 Ma to ~24.0 Ma), Zone C1-D (late Chattian
147 ~24.0 Ma to ~23.0 Ma) and Zone D (Aquitania: ~23.0 Ma to ~21.0 Ma).

148 These sections form an integrated sedimentary succession with a thickness of ~115 m (Richo
149 et al., 2017). Two prominent stratigraphic marker beds, the basalt I group (32.4-29.1 Ma) and
150 the basalt II group (28.7-24.9 Ma) crop out at ~40-41 m and at ~94-100 m in the sedimentary
151 profile (Daxner-Höck et al., 2017). A younger basalt III group (13.2–12.2 Ma) dates back to

152 the middle Miocene, but is not part of the sedimentary succession investigated here. Further
153 details about the local nomenclature, the investigated profiles, profile correlation and
154 lithostratigraphic relationships are provided in Harzhauser et al. (2017), Daxner-Höck et al.
155 (2017) and Richo et al. (2017). Due to the complex architecture of the Valley of Lakes basin
156 and adjacent areas, a mixed provenance has been proposed for the basin fill, however, detailed
157 knowledge about the palaeo-depositional environment and source area relationships remain
158 poorly constrained (Höck et al., 1999).

159

160 **3. Materials and Methods**

161 3.1 Materials

162 Representative bulk sediment samples (140 in total) were taken from different outcrops, which
163 cover the entire sedimentary succession of the Valley of Lakes from the upper Eocene to the
164 lower Miocene. The layers sampled vary in color, composition, texture, fossil and carbonate
165 content, etc., however, they do not show optical signs of alteration, such as recent surface
166 weathering. Samples for geochemical, isotopic and mineralogical analysis were crushed in a
167 ball mill for 10 min and micronized using a McCrone mill for 8 min, with ethanol addition.
168 Samples with a high clay mineral content based on an initial mineralogical inspection were
169 selected further for an identification of the clay mineral suite, which is defined here as $< 2 \mu\text{m}$
170 size fraction (Rafiei et al., 2020). As for the clay mineral separation, 5 g of the bulk material
171 was reacted with 5 % HCl for 10 min to remove the carbonates, followed by standard Atterberg
172 sedimentation and subsequent collection and drying of the $< 2 \mu\text{m}$ size fraction at 40 °C. Fast
173 acid digestion was used to reduce leaching or dissolution of the clay minerals under acidic
174 conditions (Baldermann et al., 2012). Four samples from the Hsanda Gol Formation with a
175 high amount of illitic phases were used for an illite polytype and K-Ar analysis. To this end,

176 three sub-fractions (< 1 μm, 1-2 μm and 2-10 μm) were separated by Atterberg sedimentation,
177 which all represent mixtures of authigenic illitic phases and detrital illite/muscovite.

178

179 3.2 Analytical methods

180 The major, minor and trace element composition of a sub-set of samples (91 in total) was
181 analyzed via a Philips PW2404 wavelength dispersive X-ray fluorescence (XRF) spectrometer.

182 Fine powdered samples (0.8 g) were heated to 1050 °C to remove the volatile components
183 (CO₂, H₂O, etc.), following determination of the loss on ignition (LOI) by gravimetric analysis.

184 The residuals were fused at 1200 °C using LiBO₂ (4 g) as the fluent agent. The standard glass
185 tablets were analyzed together with a set of USGS standards (analytical error: ± 0.5 wt% for
186 the major elements; Richoz et al., 2017).

187 Sediment origin and variations in the detrital influx among the different provenance areas were
188 depicted using discrimination plots calculated on the basis of major oxide compositions (Roser
189 and Korsch, 1988). The weathering paths and intensities in the source rock areas were assessed
190 through changes in the weathering indices, such as the chemical index of alteration (CIA), the
191 chemical index of weathering (CIW) and the plagioclase index of alteration (PIA), which were
192 calculated based on the major oxide compositions using the following equations (Nesbitt and
193 Young, 1982; Abdullayev et al., 2021):

$$194 \text{ CIA} = (\text{Al}_2\text{O}_3 / (\text{Al}_2\text{O}_3 + \text{CaO}^* + \text{Na}_2\text{O} + \text{K}_2\text{O})) \times 100$$

$$195 \text{ CIW} = (\text{Al}_2\text{O}_3 / (\text{Al}_2\text{O}_3 + \text{CaO}^* + \text{Na}_2\text{O})) \times 100$$

$$196 \text{ PIA} = (\text{Al}_2\text{O}_3 - \text{K}_2\text{O}) / (\text{Al}_2\text{O}_3 + \text{CaO}^* + \text{Na}_2\text{O} - \text{K}_2\text{O}) \times 100,$$

197 where CaO* denotes the fraction of CaO present in the silicate fraction. CaO* was calculated
198 by subtraction of the total CaO content of the bulk sediments (determined by XRF analyses)
199 from the CaO content associated with carbonate minerals (determined by XRD analyses, see

200 below). The weathering conditions of the source areas were identified further using $\text{Al}_2\text{O}_3 -$
201 $\text{CaO}^* + \text{Na}_2\text{O} - \text{K}_2\text{O}$ (A-CN-K) ternary diagrams (Nesbitt and Young, 1984).

202 The mineralogical composition of all bulk samples was determined by Rietveld-based analysis
203 of X-ray diffraction (XRD) patterns recorded on a PANalytical X'Pert PRO diffractometer
204 (Co-K α ; 40 kV and 40 mA) equipped with a high-speed Scientific X'Celerator detector. The
205 top loading technique was used for the preparation of randomly oriented samples, which were
206 examined in the range from 4-85 2θ with $0.008^\circ 2\theta/\text{s}$ step size and 40 s count time. The
207 PANalytical X'Pert Highscore Plus software and a pdf-4 database were used for mineral
208 quantification (analytical error: < 3 wt%; Baldermann et al., 2021). The separated grain size
209 sub-fractions were X-rayed under identical operational conditions. The amounts of authigenic
210 (1M and 1M_d polytype) and detrital (2M₁ polytype) illitic phases were calculated using the
211 following equations (Grathoff and Moore, 1996):

$$212 \quad \%2M_1 = 2.05 + 360 \times A_{(114)}/A_{(2.6 \text{ \AA} \text{ band})}$$

$$213 \quad \%1M = 4.98 + 136 \times A_{(-112)}/A_{(2.6 \text{ \AA} \text{ band})}$$

$$214 \quad \%1M_d = 100 - \%1M \text{ or } 100 - \%2M_1$$

215 where A is the area (in cps·2 θ) of the polytype-specific hkl-reflections of illite and of the 2.6
216 \AA band, respectively (analytical error: $\sim \pm 5\%$; Baldermann et al., 2017).

217 Oriented clay films were prepared for the further characterization of the clay mineral fraction
218 (< 2 μm) using a Phillips PW 1830 diffractometer (Cu-K α ; 40 kV and 30 mA) outfitted with a
219 graphite monochromator and a scintillation counter. The clay films were prepared by mixing
220 50 mg of clay fraction with 5 mL of deionized water, following ultrasonic treatment in a water
221 bath for 10 min to produce a clay-in-suspension, which was subsequently sucked through a
222 porous ceramic tile of $\sim 4 \text{ cm}^2$ size (Baldermann et al., 2014). The clay films were examined in
223 the range from 3-30 $^\circ 2\theta$ with $0.02^\circ 2\theta$ step size and 2 s/step count time, each at air-dry states,
224 after solvation with ethylene glycol (EG) and after heat treatment at 550 $^\circ\text{C}$ for 1 h. The

225 proportion of illite layers (%Ilt) in mixed-layered illite-smectite (Ilt-Smc) was calculated based
226 on the position of the 002-reflections obtained from XRD patterns of EG-solvated clay films
227 ($d_{\text{EG-002}}$ in Å) following the equation (analytical precision: $\pm 5\%$; Baldermann et al., 2017):

$$228 \quad \% \text{Ilt} = 60.8 \times d_{\text{EG-002}} - 504.5.$$

229 Illite crystallization ages were calculated through coupled illite polytype and K-Ar analysis
230 carried out on the separated grain size sub-fractions. The K_2O content of these samples was
231 determined in digested aliquots (1M HF and HNO_3 mixture) in duplicate via a BWB-XP flame
232 photometer™ using 1 % CsCl as the ionization buffer and 5 % LiCl as the internal standard.
233 The Ar isotopic composition was analyzed in a stainless-steel extraction and purification line
234 connected to a Thermo Scientific ARGUS VI™ noble gas mass spectrometer operated in static
235 mode at the University of Göttingen (Germany). The radiogenic ^{40}Ar content was measured
236 using the standard isotope dilution method applying a highly enriched ^{38}Ar spike calibrated
237 against the biotite standard HD-B1. K-Ar age calculations were made based on the constants
238 recommended by the IUGS (for details see Wemmer et al., 2011). The grain size sub-fractions
239 are free of K-containing mineral phases other than mica/illite group minerals, which would
240 disturb the radiogenic K-Ar ages.

241 A scanning electron microscopy (SEM) study was carried out to characterize the mineralogy,
242 chemical composition, microfabrics and alteration patterns of the authigenic and detrital (clay)
243 minerals present in the sediments. Therefore, specimens were prepared on standard SEM stubs,
244 coated with carbon and analyzed using a GEMINI® Zeiss Ultra 55 microscope operated at 5-
245 15 kV of accelerating voltage and equipped with a high efficiency in-lens secondary electron
246 (SE) detector and an EDAX Si(Li)-detector for high-resolution imaging and energy-dispersive
247 X-ray spectrometry (EDX) analysis.

248 The $\delta^{13}\text{C}$ and $\delta^{18}\text{O}$ isotopic composition of the carbonate fraction was analyzed to constrain the
249 palaeo-climatic trends recorded in the paleosols. In a previous study (Richoz et al., 2017) it

250 was shown that the soil carbonates (calcrete nodules, lenses and crusts) mostly record pristine
251 $\delta^{13}\text{C}$ and $\delta^{18}\text{O}$ isotopic compositions reflective of conditions during their formation and are not
252 influenced by detrital or secondary carbonates, such as calcite spar or dolomite. The samples
253 (139 in total) were reacted with 102 % phosphoric acid at 70 °C in a Kiel II automated reaction
254 system and the liberated CO_2 gas analyzed with a ThermoFinnigan mass spectrometer MAT
255 Delta. The measured $\delta^{13}\text{C}$ and $\delta^{18}\text{O}$ values were corrected against the NBS19 standard and are
256 reported in per mill (‰) relative to the Vienna-PeeDee Belemnite (V-PDB) standard (analytical
257 precision: < 0.05 ‰ for $\delta^{13}\text{C}$ and < 0.1 ‰ for $\delta^{18}\text{O}$; Richoz et al., 2017).

258

259 **4. Results**

260 4.1 Sediment petrography

261 An integrated lithostratigraphic profile of the investigated sedimentary succession (upper
262 Eocene to lower Miocene) from the Taatsiin Gol region, which is a part of the Valley of Lakes,
263 including the biozonation and some field impressions, is presented in Figure 2.

264 The sediments from the Tsagaan Ovoo Formation (upper Eocene) are dominantly coarse clastic
265 sand and gravel deposits of white-greyish color with embedded clay and silt layers of greyish-
266 yellow-green to reddish-brown color, depending on the Fe content (Richoz et al., 2017). The
267 coarser beds show cross-bedding and are frequently poorly sorted, while the finer layers show
268 trough and planar cross-bedding, lamination, inverse to normal grading, rarely ripples and
269 channel fills, and are better sorted. Roots and plant debris and bioturbation features, such as
270 burrows, indicate local paleosol formation (Richoz et al., 2017).

271 The overlying Hsanda Gol Formation (Oligocene) has a higher fossil content (mainly remains
272 of small mammals) and appears as horizontally bedded and poorly sorted clay to silt layers of
273 brick-red to reddish-brown color with intercalated cross-bedded sandstone beds and minor sand
274 and granule lenses of greyish color (Fig. 2c). Paleosol formation is documented by abundant

275 crypto- to microcrystalline calcite nodules and calcite crusts of centimeter to decimeter size
276 encapsulating soil and plant materials (Fig. 2b; Richoz et al., 2017). These calcrete layers of
277 greyish-white color are partially intergrown with Fe- and Mn-(oxy)hydroxides of orange-
278 greyish-black color. The basalt I and basalt II horizons are exposed at ~40-41 m and at ~94-
279 100 m and interfinger with the sediments from the Hsanda Gol Formation (Fig. 2b,d).
280 The Loh Formation (lower Miocene) comprises generally poorly sorted and structure-less silty-
281 clayey horizons with embedded pebbles and lenses of greyish-white to reddish-brown color as
282 well as trough to planar cross-bedded sand and gravel beds of greenish-yellow-red color, which
283 are deposited in alternate mode. Sedimentary structures seen in the coarser beds include inverse
284 to normal grading, ripple marks, channel and scour fills and overbank fines (Richoz et al.,
285 2017). Most horizons are highly fossiliferous (remains of small mammals and gastropods) and
286 show signs of paleosol formation, such as calcite nodules and crusts incorporating plant debris,
287 and burrow structures (Harzhauser et al., 2017).

288

289 4.2 Bulk and clay mineralogy

290 The mineralogical composition of the Valley of Lakes samples is dominated by quartz (10-55
291 wt%), illite/muscovite (10-50 wt%), calcite (0-70 wt%), feldspar (5-15 wt%; mainly albite and
292 plagioclase and minor orthoclase) and hematite (0-10 wt%) (Table S1). XRD analysis identifies
293 the illite/muscovite as an almost pure illitic phase composed of > 95 % Ilt layers and < 5 %
294 Smc layers (Fig. S1) with the 1M_d polytype structure dominating (~90-95 % of the total illite
295 fraction; Fig. S2). The proportions of the 1M and 2M₁ polytype structures of illite do not exceed
296 ~5-10 % of the total illite fraction. Kaolinite, chlorite (Mg-rich), mixed-layered Ilt-Smc
297 comprised of ~30-10 % Ilt layers and ~70-90 % Smc layers (Fig. S1) as well as Ti-oxides (rutile
298 and anatase) represent minor constituents (Fig. S2), accounting altogether for less than ~5 wt%
299 of the sediments. Trace amounts of zeolite and amphibole (< 5 wt%) are documented between

300 ~35 and 45 m and between ~90 and 110 m in the sedimentary succession, i.e., adjacent to the
301 basalt I and II groups. Vermiculite, dolomite, ankerite, anhydrite, halite and pyrite were not
302 identified in the samples, which contrasts observations made by Höck et al. (1999).

303 The sediments from the Tsagaan Ovoo Formation have the highest proportions of quartz, illite,
304 feldspar and hematite and the lowest content of calcite compared to the other two formations,
305 consistent with less abundant calcrete horizons developed in the upper Eocene sediments (Fig.
306 3a). The sediments from the Oligocene Hsanda Gol and lower Miocene Loh formations have
307 highly variable, but on average higher calcite contents than the Tsagaan Ovoo Formation due
308 to abundant paleosol formation and related lower contents of silicate minerals and hematite
309 (Fig. 3b,c). The depletion of hematite in these samples argues for a detrital origin and for the
310 precipitation of this mineral phase on silicate detritus during sediment transportation under oxic
311 conditions. No systematic trends in the abundance of the mineral phases was observed across
312 the investigated profile (cf. Table S1).

313

314 4.3 Microfabrics and illite crystallization ages

315 A microstructural study of weakly consolidated samples taken from the Hsanda Gol Formation
316 reveals (sub)angular to rounded detrital quartz grains (Fig. S3a), which are partly overgrown
317 by diagenetic quartz cement (Fig. S3b), as well as partially dissolved feldspar grains (Fig. S3c).
318 Calichized areas are cemented by calcite spar, which appears as crypto- to microcrystalline
319 material with aggregate particle sizes in the micrometer to millimeter range (Fig. S3d). All
320 these components are covered or intergrown by fine hematite particles (Fig. S3e), although silt-
321 size hematite grains are also observable. Coarse chlorite flakes as well as tiny, rounded to
322 vermiform kaolinite particles are barely seen (Fig. S3f). Indeed, the clay mineral suite is
323 dominated by two types of illite and one type of Ilt-Smc. SEM-EDX analysis suggests the illites
324 have higher contents of Al_2O_3 and K_2O , but lower contents of SiO_2 and Na_2O than the Ilt-Smc.

325 The illites occur either as micrometer-sized particles with platy or pseudo-hexagonal forms
326 being evenly dispersed throughout the matrix (type 1: Fig. 4a,c,e,g) or as long (micrometer-
327 scale), but thin laths and fibers, which grow into the open pore space (type 2: Fig. 4b,d,f,g,h).
328 The latter type of illite is often referred to as “hairy illite” (Güven et al., 1980; Rafiei et al.,
329 2020). The Ill-Smc is a nanometer-sized material with flaky to irregular particle forms, which
330 covers detrital grains or grows into the open pore space (type 3: Fig. 4b,d,h).
331 When viewed together with the results of the illite polytype analysis and measured K-Ar ages
332 (Table 1), all sub-samples represent physical mixtures of detrital $2M_1$ illite/muscovite (type 1),
333 authigenic $1M_d/1M$ illite (type 2) and authigenic $1M_d$ Ill-Smc (type 3). Accordingly, the plot
334 of the proportion of $2M_1$ illite/muscovite against the K-Ar age of a given sub-sample (Fig. 5)
335 provides individual crystallization ages for the detrital and authigenic illitic phases (Grathoff
336 and Moore, 1996): The upper intercept of the best-fitting line at 100 % of $2M_1$ reveals the
337 crystallization age of detrital illite/muscovite, which is 727.6 to 797.9 Ma. The lower intercept
338 of the best-fitting lines at 100 % of $1M_d + 1M$ gives crystallization ages for the authigenic clay
339 minerals, which vary between 25.2 and 34.2 Ma.

340

341 4.4 Geochemistry and weathering indices

342 Variations in the major element composition of the samples (Table S2) follow changes in the
343 abundance of silicate minerals (e.g., quartz, feldspar and clay minerals) relative to calcite and
344 hematite across the sedimentary succession. No distinct trends among the different formations
345 are seen, except for a lower CaO content and higher contents of SiO_2 , Al_2O_3 , K_2O , Na_2O , MgO
346 and Fe_2O_3 , on average, in the Tsagaan Ovoo Formation, compared to the Hsanda Gol and Loh
347 formations, corroborating the mineralogical and petrographic results (cf. Table S1 and Fig. 3).
348 Minor amounts of TiO_2 belong to rutile and anatase and traces of MnO and P_2O_5 correspond
349 to Mn-oxides and apatite. The positive correlations of Cu, Ga, Rb and Zn with Al_2O_3 as well

350 as Ce, La, Y and Zr with TiO₂ and Sr with CaO point to their association with clay minerals
351 (i.e., structural incorporation or sorption onto the clay mineral surface), heavy minerals and
352 carbonate minerals, respectively (Abdullayev et al., 2021). Ba, Co, Cr, Hf, Nb, Ni, Pb, Sc, Th,
353 V and U are inconspicuous due to lack of correlation with Al₂O₃ and TiO₂ or low concentration
354 in the samples.

355 The plot of the chemical data in the A-CN-K ternary diagram (Fig. 6) shows the samples fall
356 within or plot slightly above the compositional range of Post-Archean Australian Shale (PAAS)
357 and Average Proterozoic Shale (APS) and thus follow the predicted weathering trend for basalt
358 protoliths and Upper Continental Crust (UCC) rocks (Nesbitt and Young, 1984; Bahlburg and
359 Dobrzinski, 2011). The shift of most of the data toward the K pole of the diagrams indicates
360 K-metasomatism has affected the chemical composition of the sediments through the growth
361 of authigenic illite and Ill-Smc (Fedo et al., 1995), consistent with petrographic observations
362 and clay polytype analyses. The CIA, CIW and PIA values vary from 70-83, 83-97 and 79-96
363 across the different formations, which averages of 79, 94 and 92 for the Loh Formation and 76,
364 90 and 88 for both the Hsanda Gol and Tsagaan Ovoo formations, respectively (Table S3).

365

366 4.5 Soil carbonate $\delta^{18}\text{O}$ and $\delta^{13}\text{C}$ isotopic composition

367 The $\delta^{18}\text{O}$ and $\delta^{13}\text{C}$ values of the soil carbonates vary in the range from -11.7 to -0.2 ‰ and -
368 8.1 to -3.8 ‰ across the sedimentary succession of the Valley of Lakes (Table S4). Six samples
369 taken close to the basalt I and II groups show comparatively lighter isotope values, -12.9 to -
370 8.6 ‰ of $\delta^{18}\text{O}$ and -9.4 to -8.3 ‰ of $\delta^{13}\text{C}$, which indicates post-depositional overprinting.
371 Therefore, these samples are not considered further. A high scatter in $\delta^{18}\text{O}$ values (-9.3 to -0.2
372 ‰) and relatively light $\delta^{13}\text{C}$ values (-7.5 to -6.4 ‰) are seen in the lower part of the Hsanda
373 Gol Formation, changing into less fluctuating $\delta^{18}\text{O}$ values (-10.3 to -7.0 ‰) and systematically
374 heavier $\delta^{13}\text{C}$ values (-7.6 to -3.8 ‰) in the middle and upper part of the Hsanda Gol Formation

375 until the lower Miocene. Around the series/stage boundary, a gradual shift towards lighter $\delta^{18}\text{O}$
376 values (-11.7 to -8.6 ‰) and fluctuating, but lighter $\delta^{13}\text{C}$ values (-8.1 to -4.4 ‰) are evident.

377

378 **5. Discussion**

379 5.1 Sediment provenance

380 The time interval from the Neoproterozoic to the late Permian saw the development of large parts
381 of the fault- and thrust-bounded crystalline basement of Mongolia. The main lithological units
382 forming this basement include Neoproterozoic metamorphic rocks and Palaeozoic metasediments
383 and magmatic rocks, which are all intruded by volcanic and magmatic rocks of various age,
384 composition and provenance (Zorin et al., 1993). This complex architecture and the denudation
385 processes in the Mesozoic, which formed the Valley of Lakes basin and created the present-
386 day regional landscape and relief, are documented in the heavy mineral spectra of the Cenozoic
387 basin fill (Höck et al., 1999): the presence of epidote, amphibole, garnet, rutile, pyroxene,
388 sphene, zircon and tourmaline suggest that a mountainous region in the area of the present-day
389 Khangai mountains were the potential source areas (McLennan et al., 1993). Quartz, pegmatite,
390 granite, siltstone, basalt and carbonate clasts found in the gravel fraction (Höck et al., 1999)
391 are also indicative of a heterogeneous provenance for the Valley of Lakes sediments.

392 The major oxide compositions of the sediments from the Valley of Lakes mainly plot in the
393 “P4-quartzose sedimentary provenance” field and only a few samples plot into the “P1-mafic
394 igneous provenance” field in the Roser and Korsch (1988) discrimination diagram (Fig. 7).
395 This indicates metamorphosed sediments rich in quartz and poor in feldspar and subordinate
396 mafic to intermediate igneous and metamorphic rocks are the source rocks for the Valley of
397 Lakes sediments. These rock types are common to all lithological units exposed in the adjacent
398 lands of the Valley of Lakes (Höck et al., 1999). However, if considering the crystallization
399 ages of the $2M_1$ detrital illite/muscovite (727.6 to 797.9 Ma, cf. Fig. 5), a robust assignment to

400 provenance areas in the adjacent northern Burdgol zone and Baidrag zone is possible. The
401 Burdgol zone hosts dominantly metapelites, metapsammites and metacherts, which have an
402 age of 699 ± 35 Ma, as inferred from K-Ar dating of muscovite (Teraoka et al., 1996), which
403 closely matches the detrital illite/muscovite ages measured in the sediments from the Valley of
404 Lakes. The shift towards older ages can be explained by a minor contribution of Neoproterozoic
405 rocks from the nearby Baidrag zone (~ 2.65 Ga old), which are comprised of high-grade
406 gneisses, charnockites and amphibolites. Both source areas coincide with the heavy mineral
407 spectra and gravel lithologies of the Valley of Lakes sediments (Höck et al., 1999).

408 Assuming the detrital illite/muscovite in the Valley of Lakes sediments is a mixture of eroded,
409 metamorphosed and/or intruded material from both source regions, a relative contribution of
410 $\sim > 95$ % from the Burdgol zone and $\sim < 5$ % from the Baidrag zone to the total detrital mica
411 fraction can be calculated. Detrital silicate influx from the northernmost Bayan Khongor zone,
412 Dzag zone and Khangai zone is considered to be unlikely, as these source areas are geologically
413 younger (Ordovician to Cretaceous) (Teraoka et al., 1996). Mixtures of different proportions
414 of detritus from the Burdgol zone and some younger and older material are unlikely as well, as
415 constant source proportions over time would be required to explain the same ages for the four
416 investigated samples. This assertion is consistent with the conclusion drawn by Richoz et al.
417 (2017), who have argued that the overall sedimentation system and the sediment provenance
418 areas have not significantly changed in the considered timeframe. Therefore, the source area
419 relationships of the sediments from the Valley of Lakes are less complex than previously
420 thought with most detritus delivered from the regionally adjacent northern areas located within
421 a 100 km range. Thus, variation in the chemical weathering indices outlined below most likely
422 record changes in the weathering conditions of the source rock areas rather than changes in the
423 sedimentary facies at the same time.

424

425 5.2 Depositional environment

426 The poorly sorted, massive to partly cross-bedded sand and gravel beds of the Tsagaan Owoo
427 Formation are interpreted as debris flow deposits in alluvial fans, according to the classification
428 of Miall (1996) for fluvial sediments. These were generated during or soon after heavy rainfall
429 events, which caused the water-saturated regolith to move down slope (Hubert and Filipov,
430 1989). The finer, laminated layers with ripple marks, inverse to normal grading and channel
431 fills deposited in-between the coarser clastic beds represent the background sedimentation in
432 the upper Eocene, i.e., braided river deposits developed in close vicinity to propagating alluvial
433 fans (Miall, 1996). Imbrications of pebbles, cobbles and clasts within these beds suggest a
434 palaeo-current direction from north to south (Höck et al. 1999), which is consistent with major
435 sediment source areas in the northern Burd gol Zone. In contrast to Badamgarav (1993) and
436 Daxner-Höck et al. (2017), we found no petrographic-sedimentological evidence for lake or
437 playa sedimentation in the upper Eocene strata, which we attribute to the different sample types
438 considered: While Badamgarav (1993) and Daxner-Höck et al. (2017) identified efflorescent
439 salt crusts composed of halite, tepees and polygonal structures in some sedimentary layers, no
440 such structures were observed in the paleosol horizons of the same age. However, the scatter
441 in the $\delta^{18}\text{O}$ isotopic composition of the soil carbonates, which has been attributed to varying
442 amounts of evaporation (Richoz et al., 2017), is consistent with a playa lake setting.

443 The poorly sorted, often horizontally bedded and fossiliferous clay-silt-sand(stone) beds of the
444 Hsanda Gol Formation were deposited in a complex environment: the finer beds have likely
445 been developed in ephemeral lakes or braided rivers systems draining proximal alluvial fans,
446 as indicated by the presence of channel sand bodies with basal channel scour lags and cross-
447 bedded sand fill. The sandier beds are interpreted as open steppe deposits, which have been
448 temporarily affected by ephemeral river and playa lake sedimentation (Miall, 1996), as it can
449 be inferred from occasional mud cracks and salt crusts (halite; Höck et al., 1999). On the

450 contrary, Sun and Windley (2015) have proposed an eolian origin for the Oligocene sediments
451 and interpreted them as loess deposits, which were transported by westerly winds, based on
452 REE patterns and comparison with grain size distributions obtained from recent Loess deposits
453 from Kansas (USA) and the Chinese Loess Plateau. Although we cannot exclude long-distance
454 transport and subsequent deposition of dust has contributed to at least a minor proportion to
455 the total basin fill of the Valley of Lakes, we found no petrographic evidence for any aeolian
456 influences, such as ripples, coarsening up laminae or climbing translent strata, ventifacts,
457 mud curls or even quartz grains with crescentic percussion marks (Kenig, 2006; Li et al., 2020).
458 The lithological variability of the Loh Formation (i.e., poorly sorted and highly fossiliferous
459 clay-silt-sand-gravel beds deposited in alternate mode) can be best explained by a combination
460 of debris flow deposits in alluvial fans (coarse clastic material) and abandoned channel deposits
461 and waning flood sedimentation (fine clastic material) of a shallow, perennial flowing braided
462 river system Miall (1996). Imbrication of gravels and flow structures in the basalt III group still
463 indicate a palaeo-current direction from north to south (Höck et al., 1999), which suggests the
464 Burdgol Zone is the main source area at least up to the upper lower Miocene.

465

466 5.3 Origin of hairy illite and Ilt-Smc

467 Höck et al. (1999) and Sun and Windley (2015) have proposed an aeolian origin or a coupled
468 aeolian-fluviatile origin for the finest fraction of the Valley of Lakes sediments, while Richoz
469 et al. (2017) concluded the finest fraction is authigenic and has been formed during or shortly
470 after the flows of the different basalt groups. However, in none of the above studies radiometric
471 ages of the clay fraction have been presented to confirm their assertions. Our XRD and SEM
472 study shows the clay mineral fraction of the Oligocene Hsanda Gol Formation is dominated by
473 hairy illite and subordinate flake-shaped Ilt-Smc, which cover detrital grains or grow into the
474 pore space (Fig. 4). All these features that are typical for authigenic illitic phases (Güven et al.,

1980; Rafiei et al., 2020). The polytype analysis and K-Ar age dating reveal these illitic phases have been precipitated between 34.2 and 25.2 Ma (Fig. 5), which (within uncertainty of the K-Ar age dating method we have used here) is well within the documented intrusion ages of the basalt I group (32.4-29.1 Ma) and basalt II group (28.7-24.9 Ma) (Daxner-Höck et al., 2017) and closely matches the biozonation reported in Harzhauser et al. (2017).

The origin of Ilt-Smc in the Valley of Lakes sediments is difficult to constrain: it could have been formed during low temperature pedogenesis from smectite or kaolinite precursors of ‘zero’ age (Huggett et al., 2016), which were deposited due to wind (allochthonous clay source) or soil water (autochthonous source) action, through a dissolution-(re)precipitation mechanism. Pedogenic degradation of detrital illitic minerals to produce Ilt-Smc under acidic conditions at low temperature has also been observed (Meenakshi et al., 2020). Contrary, several published studies question a low temperature origin of Ilt-Smc in sedimentary successions: Ilt-Smc found in paleosols from the Illinois Basin was shown to be the alteration product of siliceous parental phases, which interacted with hydrothermal brines generated during burial diagenesis rather than of ancient soil formation processes (McIntosh et al., 2020). Środoń (1984) concluded that smectite and Ilt-Smc phases are relatively stable in surface-near surroundings until the elevated temperatures of deep diagenesis are reached, which is consistent with slow kinetics of smectite illitization calculated for shallow buried sediments and/or low temperature settings (Cuadros, 2006). In the case of the Valley of Lakes sediments, the relatively low Ilt content in Ilt-Smc (~10-30 % Ilt layers) and the stratigraphic age-progression of the authigenic illitic phases up-section in the sedimentary succession may indicate a pedogenic origin of the Ilt-Smc.

Contrary to the Ilt-Smc, a pedogenic origin of the hairy illite is unlikely, because the formation of this mineral phase requires temperatures well around 100 °C (Güven et al., 1980; Nadeau et al. 1985; Baldermann et al., 2017), which is unrealistic high to occur in a developing soil profile that has experienced a maximum burial depth of only a few hundred meters (Richoiz et al.,

2017). The high Ill content (> 95 % Ill layers) and the hairy appearance of the illite argue for a formation at elevated temperatures, which likely developed simultaneously or shortly after the prominent and recurrent basalt flows, consistent with a basalt-mediated diagenesis. Under such conditions, pore fluids rich in K^+ , Al^{3+} and silicic acid are generated through the dissolution of unstable components, such as feldspar, which subsequently infiltrated the poorly consolidated (porous) Valley of Lakes sediments, thereby promoting the direct precipitation and growth of hairy illite in open pores (Fig. 4) and/or the hydrothermal alteration of pre-existing pedogenic Ill-Sem to hairy illite (Baldermann et al., 2017). This mechanism is applicable to explain the shift of the chemical data towards the K pole in the A-CN-K ternary diagram (Fig. 6).

509

510 5.5. Palaeo-climate and weathering conditions

511 Climatic conditions are a primary control of the intensity and type of terrestrial weathering
512 processes, where humid periods favor chemical weathering and arid periods favor physical
513 weathering (Chamley, 1989). Analogously, hydroclimatic conditions take a key control on the
514 intensity of pedogenic processes, which can be recorded in the $\delta^{13}C$ and $\delta^{18}O$ isotopic signature
515 of authigenic carbonates (i.e., calcrete in paleosols), where wetter conditions favor an excursion
516 towards lighter $\delta^{13}C$ and $\delta^{18}O$ values and drier conditions favor an excursion towards heavier
517 $\delta^{13}C$ and $\delta^{18}O$ values (Richoz et al., 2017). Hence, variations in chemical weathering indicators
518 (CIA, PIA and CIW) and in the $\delta^{13}C$ and $\delta^{18}O$ profiles of soil carbonates across a sedimentary
519 succession can be used to trace and assess fluctuations in the climatic conditions that prevailed
520 in the source areas and in the sedimentary basin at the time of sediment deposition, and during
521 pedogenesis (Nesbitt and Young, 1982; Bahlburg and Dobrzinski, 2011; Fischer-Femal and
522 Bowen, 2020; Kelson et al., 2020; Zamanian et al., 2021). The formation of soil carbonates is
523 a highly complex process that can complicate the interpretation of their $\delta^{13}C$ and $\delta^{18}O$ isotopic
524 values (Richoz et al., 2017), as global climatic trends may be overprinted by regional factors,

525 such as contamination with detrital carbonates, dolomitization, meteoric diagenesis, maturation
526 or oxidation of organic matter, dis-equilibrium conditions between atmospheric (or biogenic)
527 CO₂ and soil solution, evaporation, basalt hydrothermalism, etc. (Kaufman and Knoll, 1995;
528 Kent-Corson et al., 2009; Caves et al., 2014; Li et al., 2016; Baldermann et al., 2020; Li et al.,
529 2020). However, if considering that the pristine soil carbonate $\delta^{13}\text{C}$ and $\delta^{18}\text{O}$ isotopic signature
530 is almost well preserved in the Valley of Lakes sediments, their use for palaeo-environmental
531 reconstructions is possible.

532 The analysis of the $\delta^{13}\text{C}$ and $\delta^{18}\text{O}$ isotopic profiles recorded in the soil carbonates from the
533 Valley of Lakes (~34-21 Ma) yielded the following palaeo-climatic trends, which are consistent
534 with inverse shifts seen in the chemical weathering indices (dashed orange lines in Fig. 8), i.e.,
535 periods with increased precipitation coincide with higher chemical weathering indices and vice
536 versa. This inverse relation is a robust recorder of changing humid/arid climatic conditions in
537 an overall arid climate through the Cenozoic in Central Asia, if considering that the source
538 areas providing the silicate detritus have not changed over time in the investigated sedimentary
539 succession and that a stable sedimentation system had been established. Thus, changes in the
540 sedimentary facies, post-diagenetic impacts, basalt flow events or regional tectonic activities are
541 only barely seen in the soil carbonate $\delta^{13}\text{C}$ and $\delta^{18}\text{O}$ isotopic profiles. Accordingly, during the
542 late Eocene to the earliest Oligocene comparatively humid to semi-arid climatic conditions
543 prevailed in Central Asia (phase i); biozone A to bottom part of biozone B; ~34-31 Ma), which
544 is followed by an early Oligocene aridification (phase ii); bottom part of biozone B; ~31 Ma)
545 and the establishment of more arid climatic conditions afterwards until the terminal Oligocene
546 (phase iii); upper part of biozone B to biozone C1-D; ~31-23.5 Ma). A shift back towards
547 comparatively humid to semi-arid climatic conditions is evident in the late Oligocene to earliest
548 Miocene (phase iv); transition between biozones C1-D and D; ~23.5-23 Ma), which is followed
549 by the establishment of these conditions in the early Miocene (phase v); biozone D; ~23-21

550 Ma). We note here that the atmospheric CO₂ concentration decreased from 800 ppm to 200
551 ppm from ~33 to 22 Ma (Zhang et al., 2013), which should have shifted the soil carbonate δ¹³C
552 signatures towards lighter values. However, due to changes in aridification in Central Mongolia
553 at the same time, this trend is not seen in the data. Indeed, an increase in aridification results in
554 a restricted soil moisture content that can i) increase the δ¹³C value of soil carbonates, ii) causes
555 the plant productivity to decrease, which affects the ratio of atmospheric CO₂ to soil respired
556 CO₂ and iii) reduce the formation depth of the soil carbonates and thus the relative contributions
557 of atmospheric CO₂ and soil-derived carbon (Cerling and Quade 1993; Caves et al. 2014). As
558 a consequence, the δ¹³C isotopic signature of the soil carbonate is linked to aridification pulses,
559 which also affects the weathering intensity of the sediment source areas, explaining the inverse
560 relation between the isotope record and the chemical alteration indices. On the contrary, large
561 changes in the δ¹⁸O isotopic record of pristine soil carbonates are not to be expected given that
562 the hydroclimatic variations are small in the semi-arid setting of the Valley of Lakes and that
563 most moisture is recycled (Caves et al., 2015; Chamberlain et al., 2014; Kukla et al., 2019;
564 Winnick et al., 2014).

565 Global cooling events established from δ¹³C and δ¹⁸O isotope records of marine deep-sea
566 sediments (Zachos et al., 2001; Gallagher et al., 2020), such as the Oi-1a/b Glaciation (~34-33
567 Ma) or the Oligocene Glacial Maximum (~28 Ma) are barely recorded in the soil carbonate
568 δ¹³C and δ¹⁸O isotope profiles. However, they are visible by increases in chemical weathering
569 indices at exactly these time intervals (blue bars and arrows in Fig. 8) and correspond to
570 important faunal turnovers (Harzhauser et al., 2016). The early Oligocene aridification (~31
571 Ma) is seen by an excursion towards heavier isotopic values between ~55 and 60 m in the rock
572 record, but do not correspond to an important faunal turnover (Harzhauser et al., 2016). On the
573 contrary, the Oligocene warming event (~25 Ma), marked by an important extinction of the
574 mammal community, is not seen in the δ¹³C and δ¹⁸O isotopic profiles. However, in the interval

575 from ~87 to 92 m (upper part of biozone C1) an increase of all chemical weathering indices is
576 evident, which we attribute to strong illitization and local overprinting of the pristine chemical
577 signature of these sediments. The following Mi-1 Glaciation (~23 Ma) records high chemical
578 weathering patterns, but shows the expected excursion towards lighter $\delta^{13}\text{C}$ and $\delta^{18}\text{O}$ isotopic
579 values.

580 The reasons for the Cenozoic climate change are hotly debated in the literature, but a strong
581 decrease in atmospheric pCO_2 (Pagani et al., 2011; Anagnostou et al., 2016), major tectonic
582 events, such as the collision of India with Asia and progressing exhumation of the Himalaya,
583 as well as re-adjustments in oceanic gateway configurations are widely considered to have
584 altered the global ocean/atmosphere circulation patterns (Caves Rugestein and Chamberlain,
585 2018). This resulted in large-scale shifts in Earth's climate at this time, which expressed, for
586 example, in the formation and expansion of the Antarctica ice-sheets and periods of intensified
587 chemical weathering on land (Zachos et al., 2001, and references therein).

588

589 5.6 Hydroclimate and tectonics evolution in Central Asia

590 The links between the regional tectonic evolution and climate change in Central Asia have been
591 extensively studied over the past decades. Recently, Caves Rugestein and Chamberlain (2018)
592 have concluded Central Asia has received moisture through the mid-latitude westerlies,
593 maintaining stable semi-arid to arid climatic conditions ever since the early Eocene, based on
594 the analysis of $\delta^{18}\text{O}$ and $\delta^{13}\text{C}$ isotope systematics of more than 7700 terrestrial authigenic
595 carbonate samples from across Asia. On the contrary, southern Tibet, the central Tibetan
596 Plateau, China and India dominantly received southerly monsoonal moisture, favoring more
597 humid climatic conditions in these regions compared to Central Asia (Ingalls et al., 2018;
598 Sandeep et al., 2018). Our data support this viewpoint: consistently higher $\delta^{18}\text{O}$ and $\delta^{13}\text{C}$ values
599 measured for the soil carbonates from the Valley of Lakes (Fig. 8), compared to the surrounding

600 regions, indicate less precipitation and long-term, sustained arid climatic conditions prevailed
601 in the late Eocene until the early Miocene (Cerling and Quade, 1993; Kent-Corson et al., 2009;
602 Takeuchi et al., 2010; Caves et al., 2015; Li et al., 2016; Caves Rügenstein and Chamberlain,
603 2018). An influence of the height and extension of the Tibetan Plateau or the retreat of the
604 Paratethys on the hydroclimate in Central Asia at this time (An et al., 2001; Zhang et al., 2009)
605 is barely documented in the sedimentary record of the Valley of Lakes, but cannot be excluded,
606 which would express in monsoon-dominant environmental pattern and varying amounts of
607 precipitation (Zhang et al., 2013).

608 The increase in the $\delta^{13}\text{C}$ values of the soil carbonates in the Oligocene and the decrease in the
609 $\delta^{18}\text{O}$ values in the terminal Oligocene are ultimately linked to coupled effects arising from the
610 Cenozoic global cooling and the uplift of the Tian Shan and Altai from the early Neogene
611 onward, which caused changes in the seasonality and quantity of precipitation (Hendrix et al.,
612 1994; Macaulay et al., 2016; Hellwig et al., 2017; Wang et al., 2020). The resultant effects on
613 the fractionation of $\delta^{18}\text{O}$ and $\delta^{13}\text{C}$ isotopes in soil carbonates are detailed in Caves Rügenstein
614 and Chamberlain (2018), but are directly related to the development and the establishment of
615 the Altai rain shadow front. As a consequence, on the leeward side of the Altai, sustained, long-
616 term drying occurred, which is expressed by systematic changes seen in the isotope profiles
617 and chemical weathering indices (Fig. 8). Moreover, the progressive uplifting of the Hangay
618 mountains to the north ever since the early Oligocene also blocked Siberian moisture transport
619 to the northern Gobi, as it can be inferred from $\delta^{13}\text{C}$ and $\delta^{18}\text{O}$ isotope signatures recorded in
620 paleosol carbonates from different transects at the northern edge of the Gobi Desert and in the
621 lee of the Altai and Hangay mountains, and consequently contributed to the aridification of this
622 area (Caves et al., 2014; Sahagian et al., 2016; McDannell et al., 2018). This aridification led
623 to a concurrent extension of the Gobi Desert, causing shifts and turnovers in mammalian and
624 gastropod assemblages observed in soils of western Mongolia and in the adjacent eastern

625 Valley of Lakes basin at this time (Neubauer et al., 2013; Harzhauser et al., 2017; Barbolini et
626 al., 2020). We conclude the climatic and environmental evolution of Central Asia in the
627 Cenozoic was closely coupled to global climate change, regional tectonic events and adaptations
628 of the circulation pattern of the westerly winds, transporting less moisture to continental
629 Mongolia, which favored aridification.

630

631 **Acknowledgements**

632 The authors acknowledge M. Hierz, J. Jernej, S. Perchthold and A. Wolf (Graz University of
633 Technology) and S. Šimić (Institute for Electron Microscopy and Nanoanalysis and Graz
634 Centre for Electron Microscopy), who assisted us with the preparation and analysis of the
635 samples. R. Quezada-Hinojosa is greatly acknowledged for drawing the lithostratigraphic
636 profile and for providing the oxygen and carbon isotopic data. This research was funded by the
637 NAWI Graz Geocenter (Graz University of Technology). Field work and sample acquisition
638 was supported by the Austrian Science Fund (FWF) via P-23061-N19 to G. Daxner-Höck. We
639 thank our Mongolian and European team members for manifold support during the field work.

640

641 **Author contributions**

642 A.B. wrote the manuscript. W.E.P. carried out field work and collected the samples. O.W. and
643 S.R. provided the mineralogical and geochemical data. E.A. conducted the discriminant
644 function analyses. K.W. provided the K/Ar ages. A.B., S.B., S.L., W.E.P. and S.R.
645 characterized the palaeo-environment and interpreted the stable $\delta^{13}\text{C}$ and $\delta^{18}\text{O}$ isotope records.
646 All authors contributed to the writing of the manuscript.

647

648 **Additional information**

649 Supplementary materials are provided in the electronic appendix to this paper. Requests for
650 materials and correspondence should be addressed to A.B.

651

652 **Competing interests**

653 All authors declare no competing interests.

654

655 **References**

- 656 Abdullayev, E., Baldermann, A., Warr, L.N., Grathoff, G., and Taghiyeva, Y.: New constraints
657 on the palaeo-environmental conditions of the Eastern Paratethys: Implications from the
658 Miocene Diatom Suite (Azerbaijan). *Sed. Geol.*, 411, 105794,
659 <https://doi.org/10.1016/j.sedgeo.2020.105794>, 2021.
- 660 An, Z., Kutzbach, J.E., Prell, W.L., and Porter, S.C.: Evolution of Asian monsoons and phased
661 uplift of the Himalaya-Tibetan plateau since Late Miocene times. *Nature*, 411, 62-66,
662 <https://doi.org/10.1038/35075035>, 2001.
- 663 Anagnostou, E., John, E.H., Edgar, K.M., Foster, G.L., Ridgwell, A., Inglis, G.N., Pancost,
664 R.D., Lunt, D.J., and Pearson, P.N.: Changing atmospheric CO₂ concentration was the
665 primary driver of early Cenozoic climate. *Nature*, 533, 380-384,
666 <https://doi.org/10.1038/nature17423>, 2016.
- 667 Badamgarav, D.: A brief lithologo-genetic characteristics of Eocene-Oligocene and Miocene
668 deposits of the Valley of Lakes and Begger depression. In Barsbold, R., and Akhmetiev,
669 M. A. (Eds.). *International Geological Correlation Programme, Project 326 Oligocene-*
670 *Miocene Transitions in the Northern Hemisphere, Excursion Guide-Book Mongolia:*
671 *Oligocene-Miocene Boundary in Mongolia*, 36-39, 1993.
- 672 Bahlburg, H., and Dobrzinski, N.: A review of the Chemical Index of Alteration (CIA) and its
673 application to the study of Neoproterozoic glacial deposits and climate transitions. In
674 Arnaud, E., Halverson, G.P., and Shields-Zhou, G. (Eds.). *The Geological Record of*
675 *Neoproterozoic Glaciations. Chapter 6*, *Geol. Soc. Lond. Mem.*, 36, 81-92,
676 <https://doi.org/10.1144/M36.6>, 2011.
- 677 Baldermann, A., Grathoff, G.H., and Nickel, C.: Micromilieu controlled glauconitization in
678 fecal pellets at Oker (Central Germany). *Clay Miner.*, 47, 513-538,
679 <https://doi.org/10.1180/claymin.2012.047.4.09>, 2012.
- 680 Baldermann, A., Reinprecht, V., and Dietzel, M.: Chemical weathering and progressing
681 alteration as possible controlling factors for creeping landslides. *Sci. Total Environ.*, 778,
682 146300, <https://doi.org/10.1016/j.scitotenv.2021.146300>, 2021.
- 683 Baldermann, A., Dohrmann, R., Kaufhold, S., Nickel, C., Letofsky-Papst, I., and Dietzel, M.:
684 The Fe-Mg-saponite solid solution series – a hydrothermal synthesis study. *Clay Miner.*,
685 49, 391-415, <https://doi.org/10.1180/claymin.2014.049.3.04>, 2014.
- 686 Baldermann, A., Dietzel, M., Mavromatis, V., Mittermayr, F., Warr, L.N., and Wemmer, K.:
687 The role of Fe on the formation and diagenesis of interstratified glauconite-smectite and
688 illite-smectite: A case study of Upper Cretaceous shallow-water carbonates. *Chem. Geol.*,
689 453, 21-34, <https://doi.org/10.1016/j.chemgeo.2017.02.008>, 2017.
- 690 Baldermann, A., Mittermayr, F., Bernasconi, S.M., Dietzel, M., Grengg, C., Hippler, D., Kluge,
691 T., Leis, A., Lin, K., Wang, X., Zünterl, A., and Boch, R.: Fracture dolomite as an archive

692 of continental palaeo-environmental conditions. *Commun. Earth Environ.*, 1, 35,
693 <https://doi.org/10.1038/s43247-020-00040-3>, 2020.

694 Barbolini, N., Woutersen, A., Dupont-Nivet, G., Silvestro, D., Tardif, D., Coster, P.M.C.,
695 Meijer, N., Chang, C., Zhang, H.-X., Licht, A., Rydin, C., Koutsodendris, A., Han, F.,
696 Rohrmann, A., Liu, X.-J., Zhang, Y., Donnadiou, Y., Fluteau, F., Ladant, J.-B., Le Hir, G.,
697 and Hoorn, C.: Cenozoic evolution of the steppe-desert biome in Central Asia. *Sci. Adv.*,
698 6, 1-16, eabb8227, <https://doi.org/10.1126/sciadv.abb8227>, 2020.

699 Bosboom, R., Dupont-Nivet, G., Grothe, A., Brinkhuis, H., Villa, G., Mandic, O., Stoica, M.,
700 Huang, W., Yang, W., Guo, Z., and Krijgsman, W.: Linking Tarim sea retreat (west China)
701 and Asian aridification in the late Eocene. *Basin Res.*, 26, 621-640,
702 <https://doi.org/10.1111/bre.12054>, 2014.

703 Caves, J.K., Sjostrom, D.J., Mix, H.T., Winnick, M.J., and Chamberlain, C.P.: Aridification of
704 Central Asia and uplift of the Altai and Hangay Mountains, Mongolia: stable isotope
705 evidence. *Am. J. Sci.*, 314, 1171-1201, <https://doi.org/10.2475/08.2014.01>, 2014.

706 Caves, J.K., Winnick, M.J., Graham, S.A., Sjostrom, D.J., Mulch, A., and Chamberlain, C.P.:
707 Role of the westerlies in Central Asia climate over the Cenozoic. *Earth Planet. Sci. Lett.*,
708 428, 33-43, <https://doi.org/10.1016/j.epsl.2015.07.023>, 2015.

709 Caves Rugenstein, J.K., and Chamberlain, C.P.: The evolution of hydroclimate in Asia over
710 the Cenozoic: A stable-isotope perspective. *Earth-Sci. Rev.*, 185, 1129-1156,
711 <https://doi.org/10.1016/j.earscirev.2018.09.003>, 2018.

712 Cerling, T.E.: Late Cenozoic Vegetation Change, Atmospheric CO₂, and Tectonics. In
713 Ruddiman, W.F. (Ed.). *Tectonic Uplift and Climate Change*. Springer, Boston, MA., 313-
714 327, https://doi.org/10.1007/978-1-4615-5935-1_13, 1993.

715 Cerling, T., and Quade, J. Stable carbon and oxygen isotopes in soil carbonates. In Swart, P.,
716 Lohmann, K., McKenzie, J., and Savin, S. (Eds.). *Climate Change in Continental Isotopic*
717 *Records*. American Geophysical Union, Geophysical Monograph, 78, 217-231,
718 <https://doi.org/10.1029/GM078p0217>, 1993.

719 Cermeño, P., Falkowski, P.G., Romero, O.E., Schaller, M.F., and Vallina, S.M.: Continental
720 erosion and the Cenozoic rise of marine diatoms. *Proc. Natl. Acad. Sci. U.S.A.*, 112, 4239-
721 4244, <https://doi.org/10.1073/pnas.1412883112>, 2015.

722 Chamberlain, C.P., Winnick, M.J., Mix, H.T., Chamberlain, S.D., and Maher, K.: The impact
723 of Neogene grassland expansion and aridification on the isotopic composition of
724 continental precipitation. *Global Biogeochem. Cy.*, 28, 1-13,
725 <https://doi.org/10.1002/2014GB004822>, 2014.

726 Chamley, H.: Clay Formation Through Weathering. In *Clay Sedimentology*. Springer, Berlin,
727 Heidelberg, Germany, 21-50, https://doi.org/10.1007/978-3-642-85916-8_2, 1989.

728 Cuadros, J.: Modeling of smectite illitization in burial diagenesis environments. *Geochim.*
729 *Cosmochim. Acta*, 70, 4181-4195, <https://doi.org/10.1016/j.gca.2006.06.1372>, 2006.

730 Daxner-Höck, G., Badamgarav, D., Barsbold, R., Bayarmaa, B., Erbajeva, M., Göhlich, U.B.,
731 Harzhauser, M., Höck, V., Höck, E., Ichinnorov, N., Khand, Y., Lopez-Guerrero, P.,
732 Maridet, O., Neubauer, T., Oliver, A., Piller, W.E., Tsogtbaatar, K., and Ziegler, R.:
733 Oligocene stratigraphy across the Eocene and Miocene boundaries in the Valley of Lakes
734 (Mongolia). In Daxner-Höck, G., and Göhlich, U. (Eds.). *The Valley of Lakes in*
735 *Mongolia, a key area of Cenozoic mammal evolution and stratigraphy*. *Paleobiodivers.*
736 *Paleoenviron.*, 97, 111-218, <https://doi.org/10.1007/s12549-016-0257-9>, 2017.

737 Dupont-Nivet, G., Krijgsman, W., Langereis, C.G., Abels, H.A., Dai, S., and Fang, X.M.:
738 Tibetan plateau aridification linked to global cooling at the Eocene-Oligocene transition.
739 *Nature*, 445, 635-638, <https://doi.org/10.1038/nature05516>, 2007.

740 Fedo, C.M., Nesbitt, H.W., and Young, G.M.: Unraveling the effects of potassium
741 metasomatism in sedimentary rocks and paleosols, with implications of paleoweathering

742 conditions and provenance. *Geology*, 23, 921-924, [https://doi.org/10.1130/0091-](https://doi.org/10.1130/0091-7613(1995)023<0921:UTEOPM>2.3.CO;2)
743 7613(1995)023<0921:UTEOPM>2.3.CO;2, 1995.

744 Fischer-Femal, and B.J., Bowen, G.J.: Coupled carbon and oxygen isotope model for
745 pedogenic carbonates. *Geochim. Cosmochim. Acta*, 294, 126-144,
746 <https://doi.org/10.1016/j.gca.2020.10.022>, 2021.

747 Gallagher, S.J., Wade, B., Qianyu, L., Holdgate, G.R., Bown, P., Korasidis, V.A., Scher, H.,
748 Houben, A.J.P., McGowran, B., and Allan, T.: Eocene to Oligocene high paleolatitude
749 neritic record of Oi-1 glaciation in the Otway Basin southeast Australia. *Glob. Planet.*
750 *Change*, 103218, <https://doi.org/10.1016/j.gloplacha.2020.103218>, 2020.

751 Grathoff, G.H., and Moore, D.M.: Illite Polytype Quantification Using Wildfire© Calculated
752 X-Ray Diffraction Patterns. *Clays Clay Miner.*, 44, 835-842,
753 <https://doi.org/10.1346/CCMN.1996.0440615>, 1996.

754 Guo, Z.T., Sun, B., Zhang, Z.S., Peng, S.Z., Xiao, G.Q., Ge, J.Y., Hao, Q.Z., Qiao, Y.S., Liang,
755 M.Y., Liu, J.F., Yin, Q.Z., and Wei, J.J.: A major reorganization of Asian climate by the
756 early Miocene. *Clim. Past*, 4, 153-174, <https://doi.org/10.5194/cp-4-153-2008>, 2008.

757 Güven, N., Hower, W.F., and Davies, D.K.: Nature of authigenic illites in sandstone reservoirs.
758 *J. Sed. Res.*, 50, 761-766, [https://doi.org/10.1306/212F7ADB-2B24-11D7-](https://doi.org/10.1306/212F7ADB-2B24-11D7-8648000102C1865D)
759 8648000102C1865D, 1980.

760 Harzhauser, M., Daxner-Höck, G., López-Guerrero, P., Maridet, O., Oliver, A., Piller, W.E.,
761 Richoz, S., Erbajeva, M.A., and Göhlich, U.B.: The stepwise onset of the Icehouse world
762 and its impact on Oligocene-Miocene Central Asian mammal communities. *Sci. Rep.*, 6,
763 36169, <https://doi.org/10.1038/srep36169>, 2016.

764 Harzhauser, M., Daxner-Höck, Erbajeva, M.A., G., López-Guerrero, P., Maridet, O., Oliver,
765 A., Piller, W.E, Göhlich U.B., and Ziegler, R.: Oligocene and early Miocene
766 biostratigraphy of the Valley of Lakes in Mongolia. In Daxner-Höck, G., and Göhlich, U.
767 (Eds.). *The Valley of Lakes in Mongolia, a key area of Cenozoic mammal evolution and*
768 *stratigraphy. Palaeobiodivers. Palaeoenviro.*, 97, 219-231,
769 <https://doi.org/10.1007/s12549-016-0264-x>, 2017.

770 Hellwig, A., Voigt, S., Mulch, A., Frisch, K., Bartenstein, A., Pross, J., Gerdes, A., and Voigt,
771 T.: Late Oligocene–early Miocene humidity change recorded in terrestrial sequences in
772 the Ili Basin (south-eastern Kazakhstan, Central Asia). *Sedimentology*, 65, 517-539,
773 <https://doi.org/10.1111/sed.12390>, 2017.

774 Hendrix, M., Dumitru, T., and Graham, S.: Late Oligocene-early Miocene unroofing in the
775 Chinese Tian Shan: An early effect of the India-Asia collision. *Geology*, 22, 487-490,
776 [https://doi.org/10.1130/0091-7613\(1994\)022<0487:LOEMUI>2.3.CO;2](https://doi.org/10.1130/0091-7613(1994)022<0487:LOEMUI>2.3.CO;2), 1994.

777 Höck, V., Daxner-Höck, G., Schmid, H.P., Badamgarav, D., Frank, W., Furtmüller, G.,
778 Montag, O., Barsbold, R., Khand, Y., and Sodov, J.: Oligocene-Miocene sediments, fossils
779 and basalt from the Valley of Lakes (Central Mongolia) – an integrated study. *Mitt. Österr.*
780 *Geol. Ges.*, 90, 83-125, 1999.

781 Houben, A.J.P., Bijl, P.K., Pross, J., Bohaty, S.M., Passchier, S., Stickley, C.E., Röhl, U.,
782 Sugisaki, S., Tauxe, L., van de Flierdt, T., Olney, M., Sangiorgi, F., Sluijs, A., Escutia, C.,
783 and Brinkhuis, H. et al.: Reorganization of Southern Ocean plankton ecosystem at the
784 onset of Antarctic glaciation. *Science*, 340, 341-344,
785 <https://doi.org/10.1126/science.1223646>, 2013.

786 Hubert, J.F., and Filipov, A.J.: Debris-flow deposits in alluvial fans on the west flank of the
787 White Mountains, Owens Valley, California, U.S.A. *Sed. Geol.*, 61, 177-205,
788 [https://doi.org/10.1016/0037-0738\(89\)90057-2](https://doi.org/10.1016/0037-0738(89)90057-2), 1989.

789 Huggett, J., Cuadros, J., Gale, A.S., Wray, D., and Adetunji, J.: Low temperature, authigenic
790 illite and carbonates in a mixed dolomite-clastic lagoonal and pedogenic setting, Spanish

791 Central System, Spain. *Appl. Clay Sci.*, 132-133, 296-312,
792 <https://doi.org/10.1016/j.clay.2016.06.016>, 2016.

793 Ingalls, M., Rowley, D.B., Olack, G., Currie, B.S., Li, S., Schmidt, J.L., Tremblay, M.M.,
794 Polissar, P.J., Shuster, D.L., Lin, D., and Colman, A.S.: Paleocene to Pliocene high
795 elevation of southern Tibet: Implications for tectonic models of India-Asia collision,
796 Cenozoic climate, and geochemical weathering. *Geol. Soc. Am. Bull.*, 130, 307-330,
797 <https://doi.org/10.1130/B31723.1>, 2018.

798 Kaufman, A.J., and Knoll, A.H.: Neoproterozoic variations in the C-isotopic composition of
799 seawater: stratigraphic and biogeochemical implications. *Precambrian Res.*, 73, 27-49,
800 [https://doi.org/10.1016/0301-9268\(94\)00070-8](https://doi.org/10.1016/0301-9268(94)00070-8), 1995.

801 Kelson, J.R., Huntington, K.W., Breecker, D.O., Burgener, L.K., Gallagher, T.M., Hoke, G.D.,
802 and Petersen, S.V.: A proxy for all seasons? A synthesis of clumped isotope data from
803 Holocene soil carbonates. *Quat. Sci. Rev.*, 234, 106259,
804 <https://doi.org/10.1016/j.quascirev.2020.106259>, 2020.

805 Kenig, K.: Surface microtextures of quartz grains from Vistulian loesses from selected profiles
806 of Poland and some other countries. *Quat. Int.*, 152-153, 118-135,
807 <https://doi.org/10.1016/j.quaint.2005.12.015>, 2006.

808 Kent-Corson, M.L., Ritts, B.D., Zhuang, G., Bovet, P.M., Graham, S.A., and Chamberlain,
809 C.P.: Stable isotopic constraints on the tectonic, topographic, and climatic evolution of the
810 northern margin of the Tibetan Plateau. *Earth Planet. Sci. Lett.*, 282, 158-166,
811 <https://doi.org/10.1016/j.epsl.2009.03.011>, 2009.

812 Komar, N., and Zeebe, R.E.: Reconciling atmospheric CO₂, weathering, and calcite
813 compensation depth across the Cenozoic. *Sci. Adv.*, 7, eabd4876,
814 <https://doi.org/10.1126/sciadv.abd4876>, 2021.

815 Kukla, T., Winnick, M.J., Maher, K., Ibarra, D.E., and Chamberlain, C.P.: The Sensitivity of
816 Terrestrial $\delta^{18}\text{O}$ Gradients to Hydroclimate Evolution. *J. Geophys. Res. Atmos.*, 124, 563-
817 582, <https://doi.org/10.1029/2018JD029571>, 2019.

818 Lear, C.H., Bailey, T.R., Pearson, P.N., Coxall, H.K., and Rosenthal, Y.: Cooling and ice
819 growth across the Eocene-Oligocene transition. *Geology*, 36, 251-254,
820 <https://doi.org/10.1130/G24584A.1>, 2008.

821 Li, B., Sun, D., Wang, X., Zhang, Y., Hu, W., Wang, F., Li, Z., Ma, Z., and Liang, B.: $\delta^{18}\text{O}$ and
822 $\delta^{13}\text{C}$ records from a Cenozoic sedimentary sequence in the Lanzhou Basin, Northwestern
823 China: implications for palaeoenvironmental and palaeoecological changes. *J. Asian Earth*
824 *Sci.*, 125, 22-36, <https://doi.org/10.1016/j.jseaes.2016.05.010>, 2016.

825 Li, H., Liu, X., Tripathi, A., Feng, S., Elliott, B., Whicker, C., Arnold, A., and Kelley, A.M.:
826 Factors controlling the oxygen isotopic composition of lacustrine authigenic carbonates in
827 Western China: implications for paleoclimate reconstructions. *Sci. Rep.*, 10, 16370,
828 <https://doi.org/10.1038/s41598-020-73422-4>, 2020.

829 Li, Z., Yu, X., Dong, S., Chen, Q., and Zhang, C.: Microtextural features on quartz grains from
830 eolian sands in a subaqueous sedimentary environment: A case study in the hinterland of
831 the Badain Jaran Desert, Northwest China. *Aeolian Res.*, 43, 100573,
832 <https://doi.org/10.1016/j.aeolia.2020.100573>, 2020.

833 Lu, H., Wang, X., Wang, X., Chang, X., Zhang, H., Xu, Z., Zhang, W., Wei, H., Zhang, X.,
834 Yi, S., Zhang, W., Feng, H., Wang, Y., Wang, Y., and Han, Z.: Formation and evolution
835 of Gobi Desert in central and eastern Asia. *Earth-Sci. Rev.*, 194, 251-263,
836 <https://doi.org/10.1016/j.earscirev.2019.04.014>, 2019.

837 Macaulay, E.A., Sobel, E.R., Mikolaichuk, A., Wack, M., Gilder, S.A., Mulch, A., Fortuna,
838 A.B., Hynek, S., and Apayarov, F.: The sedimentary record of the Issyk Kul basin,
839 Kyrgyzstan: climatic and tectonic inferences. *Basin Res.*, 28, 57-80,
840 <https://doi.org/10.1111/bre.12098>, 2016.

841 McDannell, K.T., Zeitler, P.K., and Idleman, B.D.: Relict Topography Within the Hangay
842 Mountains in Central Mongolia: Quantifying Long-Term Exhumation and Relief Change
843 in an Old Landscape. *Tectonics*, 37, 2531-2558, <https://doi.org/10.1029/2017TC004682>,
844 2018.

845 McIntosh, J.A., Tabor, N.J., and Rosenau, A.A.: Mixed-Layer Illite-Smectite in
846 Pennsylvanian-Aged Paleosols: Assessing Sources of Illitization in the Illinois Basin.
847 *Minerals*, 11, 108, <https://doi.org/10.3390/min11020108>, 2020.

848 McLennan, S.M.: Weathering and Global Denudation. *J. Geol.*, 101, 100th Anniversary
849 Symposium: Evolution of the Earth's Surface, 295-303,
850 <https://www.jstor.org/stable/30081153>, 1993.

851 Meenakshi, Shrivastava, J.P., and Chandra, R.: Pedogenically degenerated illite and chlorite
852 lattices aid to palaeoclimatic reconstruction for chronologically constrained (8–130 ka)
853 loess-paleosols of Dilpur Formation, Kashmir, India. *Geosci. Front.*, 11, 1353-1367,
854 <https://doi.org/10.1016/j.gsf.2019.11.007>, 2020.

855 Miall, A.D.: The geology of fluvial deposits. Berlin, Germany, Springer, 1-582,
856 <https://doi.org/10.1007/978-3-662-03237-4?nosfx=y>, 1996.

857 Mudelsee, M., Bickert, T., Lear, C.H., and Lohmann, G.: Cenozoic climate changes: A review
858 based on time series analysis of marine benthic $\delta^{18}\text{O}$ records. *Rev. Geophys.*, 52, 333-374,
859 <https://doi.org/10.1002/2013RG000440>, 2014.

860 Mutz, S.G., Ehlers, T.A., Werner, M., Lohmann, G., Stepanek, C., and Li, J.: Estimates of late
861 Cenozoic climate change relevant to Earth surface processes in tectonically active orogens.
862 *Earth Surf. Dynam.*, 6, 271-301, <https://doi.org/10.5194/esurf-6-271-2018>, 2018.

863 Nadeau, P.H., Wilson, M.J., McHardy, W.J., and Tait, J.M.: The conversion of smectite to illite
864 during diagenesis: evidence from some illitic clays from bentonites and sandstones.
865 *Mineral. Mag.*, 49, 393-400, <https://doi.org/10.1180/minmag.1985.049.352.10>, 1985.

866 Neubauer, T.A., Harzhauser, M., Daxner-Höck, G., and Piller, W.E.: New data on the terrestrial
867 gastropods from the Oligocene-Miocene transition in the Valley of Lakes, Central
868 Mongolia. *Paleontol. J.*, 47, 374-385, <https://doi.org/10.1134/S003103011304014X>, 2013.

869 Nesbitt, H.W., and Young, G.M.: Early Proterozoic climate and plate motions inferred from
870 major element chemistry of lutites. *Nature*, 299, 715-717,
871 <https://doi.org/10.1038/299715a0>, 1982.

872 Nesbitt, H.W., and Young, G.M.: Prediction of some weathering trends of plutonic and
873 volcanic rocks based on thermodynamic and kinetic considerations. *Geochim.*
874 *Cosmochim. Acta*, 48, 1523-1534, [https://doi.org/10.1016/0016-7037\(84\)90408-3](https://doi.org/10.1016/0016-7037(84)90408-3), 1984.

875 Norris, R., Turner, S.K., Hull, P.M., and Ridgwell, A.: Marine Ecosystem Responses to
876 Cenozoic Global Change. *Science*, 341, 492-498,
877 <https://doi.org/10.1126/science.1240543>, 2013.

878 Pagani, M., Huber, M., Liu, Z., Bohaty, S.M., Henderiks, J., Sijp, W.P., Krishnan, S., and
879 DeConto, R.M.: The Role of Carbon Dioxide During the Onset of Antarctic Glaciation.
880 *Science*, 334, 6060, 1261-1264, <https://doi.org/10.1126/science.1203909>, 2011.

881 Pälike, H., Norris, R.D., Herrle, J.O., Wilson, P.A., Coxall, H.K., Lear, C., H., Shackleton, N.J.,
882 Tripathi, A.K., and Wade, B.S.: The heartbeat of the Oligocene climate system. *Science*,
883 314, 1894-1898, <https://doi.org/10.1126/science.1133822>, 2006.

884 Porter, T.M.: The geology, structure and mineralisation of the Oyu Tolgoi porphyry copper-
885 gold-molybdenum deposits, Mongolia: A review. *Geosci. Front.*, 7, 375-407,
886 <https://doi.org/10.1016/j.gsf.2015.08.003>, 2016.

887 Rafiei, M., Löhr, S., Baldermann, A., Webster, R., and Kong, C.: Quantitative petrographic
888 differentiation of detrital vs diagenetic clay minerals in marine sedimentary sequences:
889 Implications for the rise of biotic soils. *Precambrian Res.*, 350, 105948,
890 <https://doi.org/10.1016/j.precamres.2020.105948>, 2020.

891 Richoz, S., Baldermann, A., Frauwallner, A., Harzhauser, M., Daxner-Höck, G., Klammer, D.,
892 and Piller, W.E.: Geochemistry and mineralogy of the Oligo-Miocene sediments of the
893 Valley of Lakes, Mongolia. *Palaeobiodivers. Palaeoenviron.*, 97, 233-258,
894 <https://doi.org/10.1007/s12549-016-0268-6>, 2017.

895 Roser, B.P., and Korsch, R.J.: Provenance signatures of sandstone-mudstone suites determined
896 using discriminant function analysis of major-element data. *Chem. Geol.*, 67, 119-139,
897 [https://doi.org/10.1016/0009-2541\(88\)90010-1](https://doi.org/10.1016/0009-2541(88)90010-1), 1988.

898 Sahagian, D., Proussevitch, A., Ancuta, L.D., Idleman, B.D., and Zeitler, P.K.: Uplift of
899 Central Mongolia Recorded in Vesicular Basalts. *J. Geol.*, 124, 435-445,
900 <https://doi.org/10.1086/686272>, 2016.

901 Sandeep, S., Ajayamohan, R.S., Boos, W.R., Sabin, T.P., and Praveen, V.: Decline and
902 poleward shift in Indian summer monsoon synoptic activity in a warming climate. *Proc.*
903 *Natl. Acad. Sci. U.S.A.*, 115, 2681-2686, <https://doi.org/10.1073/pnas.1709031115>, 2018.

904 Środoń, J.: Mixed-layer illite-smectite in low-temperature diagenesis: data from the Miocene
905 of the Carpathian Foredeep. *Clay Miner.*, 19, 205-215,
906 <https://doi.org/10.1180/claymin.1984.019.2.07>, 1984.

907 Sun, J., and Windley, B.F.: Onset of aridification by 34 Ma across the Eocene-Oligocene
908 transition in Central Asia. *Geology*, 11, 1015-1018, <https://doi.org/10.1130/G37165.1>,
909 2015.

910 Takeuchi, A., Hren, M.T., Smith, S.V., Chamberlain, C.P., and Larson, P.B.: Pedogenic
911 carbonate carbon isotopic constraints on paleoprecipitation: Evolution of desert in the
912 Pacific Northwest, USA, in response to topographic development of the Cascade Range.
913 *Chem. Geol.*, 277, 323-335. <https://doi.org/10.1016/j.chemgeo.2010.08.015>, 2010.

914 Teraoka, Y., Suzuki, M., Tungalag, F., Ichinnorov, N., and Sakamaki, Y.: Tectonic framework
915 of the Bayankhongor area, west Mongolia. *Bulletin of the Geological Survey of Japan*, 47,
916 447-455, 1996.

917 Wang, X., Carrapa, B., Sun, Y., Dettman, D.L., Chapman, J.B., Rugenstein, J.K.C., Clementz,
918 M.T., DeCelles, P.G., Wang, M., Chen, J., Quade, J., Wang, F., Li, Z., Oimuhammadzoda,
919 I., Gadoev, M., Lohmann, G., Zhang, X., and Chen, F.: The role of the westerlies and
920 orography in Asian hydroclimate since the late Oligocene. *Geology*, 48, 728-732,
921 <https://doi.org/10.1130/G47400.1>, 2020.

922 Wemmer, K., Steenken, A., Müller, S., de Luchi, M.G.L., and Siegesmund, S.: The tectonic
923 significance of K/Ar illite fine-fraction ages from the San Luis formation (Eastern Sierras
924 Pampeanas, Argentina). *Int. J. Earth Sci.*, 100, 659-669, <https://doi.org/10.1007/s00531-010-0629-8>, 2011.

926 Winnick, M.J., Chamberlain, C.P., Caves, J.K., and Welker, J.M.: Quantifying the isotopic
927 “continental effect.” *Earth Planet. Sci. Lett.*, 406, 123-133,
928 <https://doi.org/10.1016/j.epsl.2014.09.005>, 2014.

929 Xiao, G.Q., Abels, H.A., Yao, Z.Q., Dupont-Nivet, G., and Hilgen, F.J.: Asian aridification
930 linked to the first step of the Eocene-Oligocene climate Transition (EOT) in obliquity-
931 dominated terrestrial records (Xining Basin, China). *Clim. Past*, 6, 501-513,
932 <https://doi.org/10.5194/cp-6-501-2010>, 2010.

933 Zachos, J., Pagani, M., Sloan, L., Thomas, E., and Billups, K.: Trends, rhythms, and aberrations
934 in global climate 65 Ma to present. *Science*, 292, 686-693,
935 <https://doi.org/10.1126/science.1059412>, 2001.

936 Zamanian, K., Lechler, A.R., Schauer, A.J., Kuzyakov, Y., and Huntington, K.W.: The $\delta^{13}\text{C}$,
937 $\delta^{18}\text{O}$ and Δ_{47} records in biogenic, pedogenic and geogenic carbonate types from paleosol-
938 loess sequence and their paleoenvironmental meaning. *Quat. Res.*, 1-17.
939 <https://doi.org/10.1017/qua.2020.109>, 2021.

940 Zhang, Y.G., Pagani, M., Liu, Z., Bohaty, S.M., and Deconto, R.: A 40-million-year history of
 941 atmospheric CO₂. *Philos. T. R. Soc. A*, 371, 20130096,
 942 <https://doi.org/10.1098/rsta.2013.0096>, 2013.

943 Zhang, C., Wang, Y., Deng, T., Wang, X., Biasatti, D., Xu, Y., and Li, Q.: C4 expansion in the
 944 central Inner Mongolia during the latest Miocene and early Pliocene. *Earth Planet. Sci.*
 945 *Lett.*, 287, 311-319, <https://doi.org/10.1016/j.epsl.2009.08.025>, 2009.

946 Zorin, Y.A., Belichenko, V.G., Turutanov, E.K., Kozhevnikov, V.M., Ruzhentsev, S.V.,
 947 Dergunov, A.B., Filippova, I.B., Tomurtogoo, O., Arvisbaatar, N., Bayasgalan, T.,
 948 Biambaa, C., and Khosbayar, P.: The South Siberia-Central Mongolia transect.
 949 *Tectonophysics*, 225, 361-378, [https://doi.org/10.1016/0040-1951\(93\)90305-4](https://doi.org/10.1016/0040-1951(93)90305-4), 1993.

950

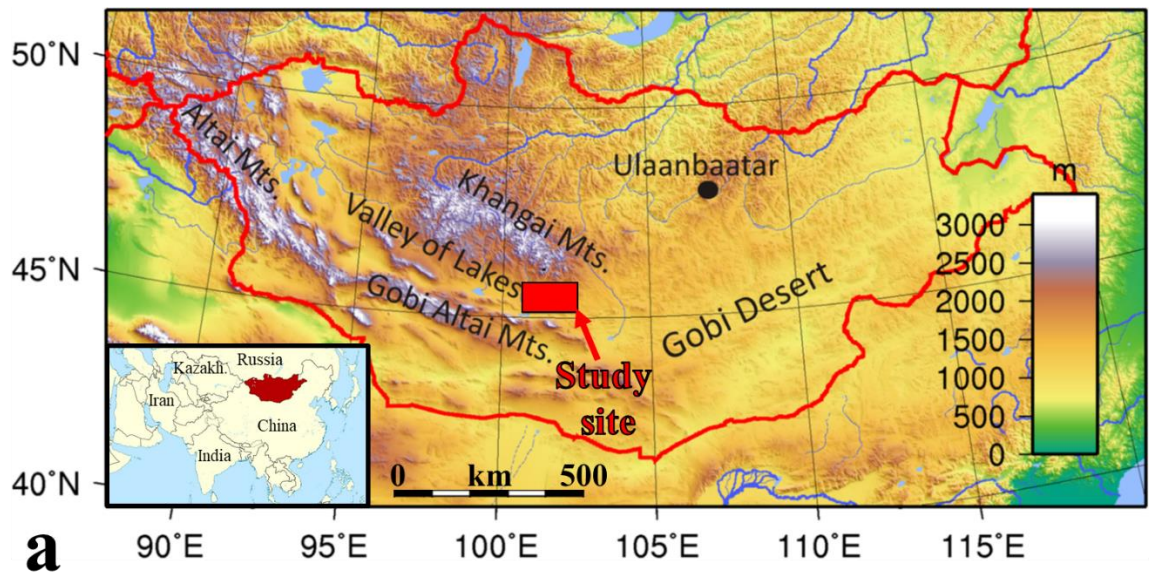
951

952 **Figure Captions / Table Captions**

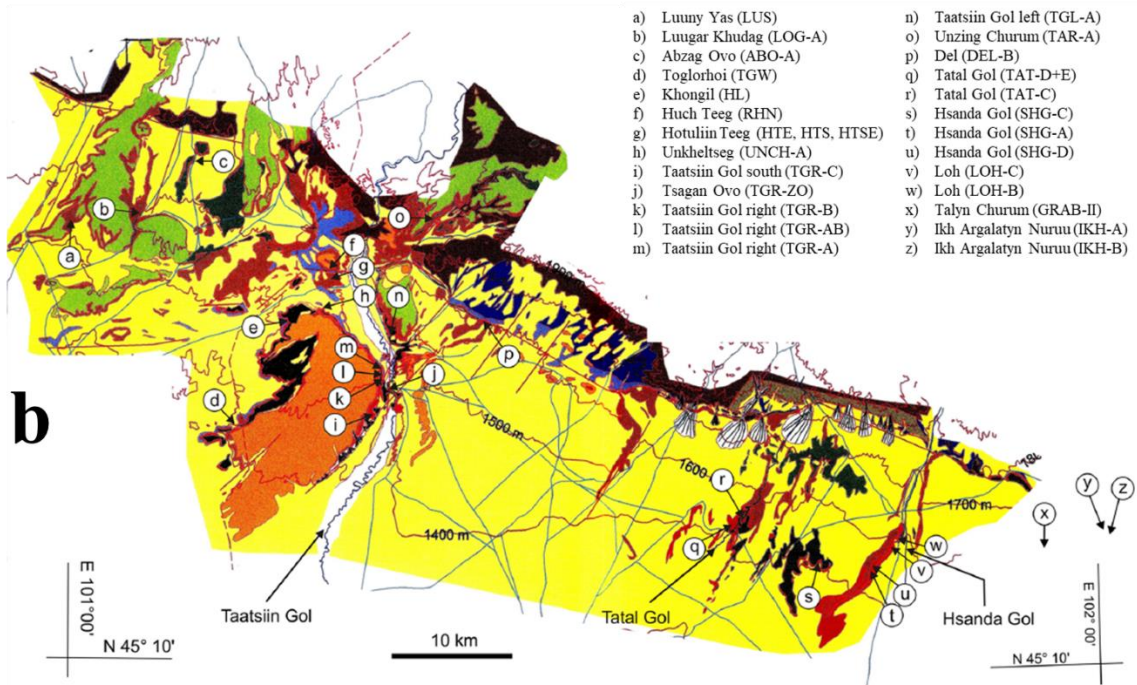
953 **Table 1:** Compilation of illite polytype quantification and K-Ar ages of grain size sub-fractions
 954 of sediments collected from (a) TAT section (~90.5 m), (b) TGR-C section (~78.0 m), (c) SHG-
 955 D section (~55.5 m) and (d) TGR-AB section (~35.0 m). The analytical error for the K-Ar age
 956 calculations is given on a 95% confidence level (2σ).

Sample	Size fraction [μm]	A ₍₋₁₁₂₎ [cps·20]	1M [%]	A ₍₁₁₄₎ [cps·20]	2M ₁ [%]	1M _d [%]	K ₂ O [wt.%]	⁴⁰ Ar* [nl/g] STP	⁴⁰ Ar* [%]	Age [Ma]	\pm 2SD [Ma]
TAT	2-10	-	-	0.054	21	79	2.59	15.45	49.05	176.1	7.1
TAT	1-2	0.006	6	0.040	16	78	2.21	11.58	77.20	155.2	2.6
TAT	< 1	0.012	7	0.023	10	83	3.39	10.75	38.18	95.8	3.2
TGR-C	2-10	-	-	0.038	16	84	2.68	13.98	81.46	155.1	2.9
TGR-C	1-2	-	-	0.031	13	87	3.64	15.80	76.96	129.6	2.4
TGR-C	< 1	0.001	5	0.027	12	95	3.10	12.88	66.83	124.6	1.9
SHG-D	2-10	-	-	0.039	16	84	2.72	14.31	78.74	156.4	2.0
SHG-D	1-2	-	-	0.034	14	86	3.86	15.93	76.09	123.6	3.2
SHG-D	< 1	0.011	6	0.016	8	94	3.49	10.38	70.94	89.9	1.3
TGR-AB	2-10	-	-	0.032	14	86	3.83	17.29	84.05	134.8	3.4
TGR-AB	1-2	-	-	0.027	12	88	3.97	16.63	84.33	125.3	1.8
TGR-AB	< 1	0.032	9	-	0	91	0.64	0.70	10.52	33.9	3.2

957



a



b

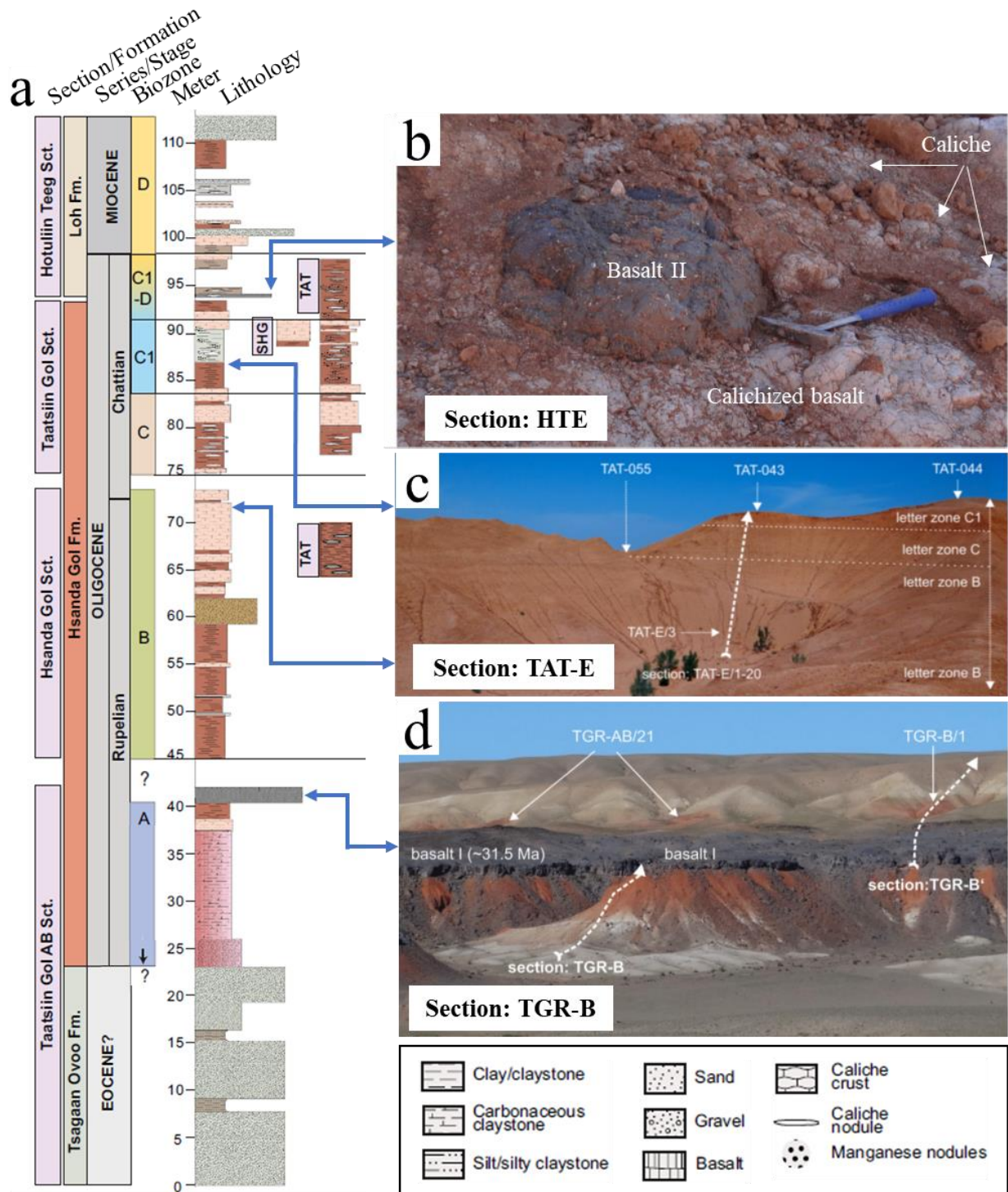
- a) Luuny Yas (LUS)
- b) Luugar Khudag (LOG-A)
- c) Abzag Ovo (ABO-A)
- d) Toglorhoi (TGW)
- e) Khongil (HL)
- f) Huch Teeg (RHN)
- g) Hotuliin Teeg (HTE, HTS, HTSE)
- h) Unkheltseg (UNCH-A)
- i) Taatsiin Gol south (TGR-C)
- j) Tsagan Ovo (TGR-ZO)
- k) Taatsiin Gol right (TGR-B)
- l) Taatsiin Gol right (TGR-AB)
- m) Taatsiin Gol right (TGR-A)
- n) Taatsiin Gol left (TGL-A)
- o) Unzing Churum (TAR-A)
- p) Del (DEL-B)
- q) Tatal Gol (TAT-D+E)
- r) Tatal Gol (TAT-C)
- s) Hsanda Gol (SHG-C)
- t) Hsanda Gol (SHG-A)
- u) Hsanda Gol (SHG-D)
- v) Loh (LOH-C)
- w) Loh (LOH-B)
- x) Talyn Churum (GRAB-II)
- y) Ikh Argalatyn Nuruu (IKH-A)
- z) Ikh Argalatyn Nuruu (IKH-B)

Legend

- | | | |
|--------------|--------------------|-------------------------|
| Quaternary | Hsanda Gol Fm. | Neoproterozoic basement |
| Tuyn Gol Fm. | Tsagan Ovo Fm. | Basalt III (M-Miocene) |
| Loh Fm. | Mesozoic sediments | Basalt I+II (Oligocene) |

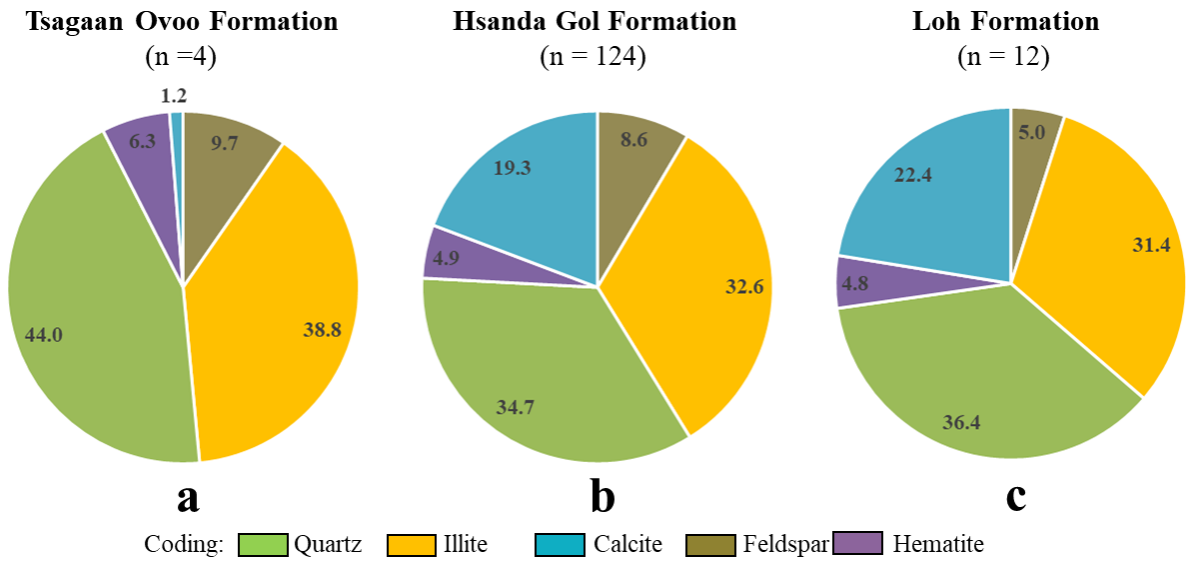
958

959 **Figure 1:** (a) Location of the study site in the Taatsiin Gol region, a part of the Valley of Lakes,
 960 in Mongolia (Central Asia). Altitude in meters is indicated on the right. (b) Geological map of
 961 the Taatsiin Gol area within the Valley of Lakes with the sampling sites marked in alphabetical
 962 order (modified after Daxner-Höck et al., 2017).



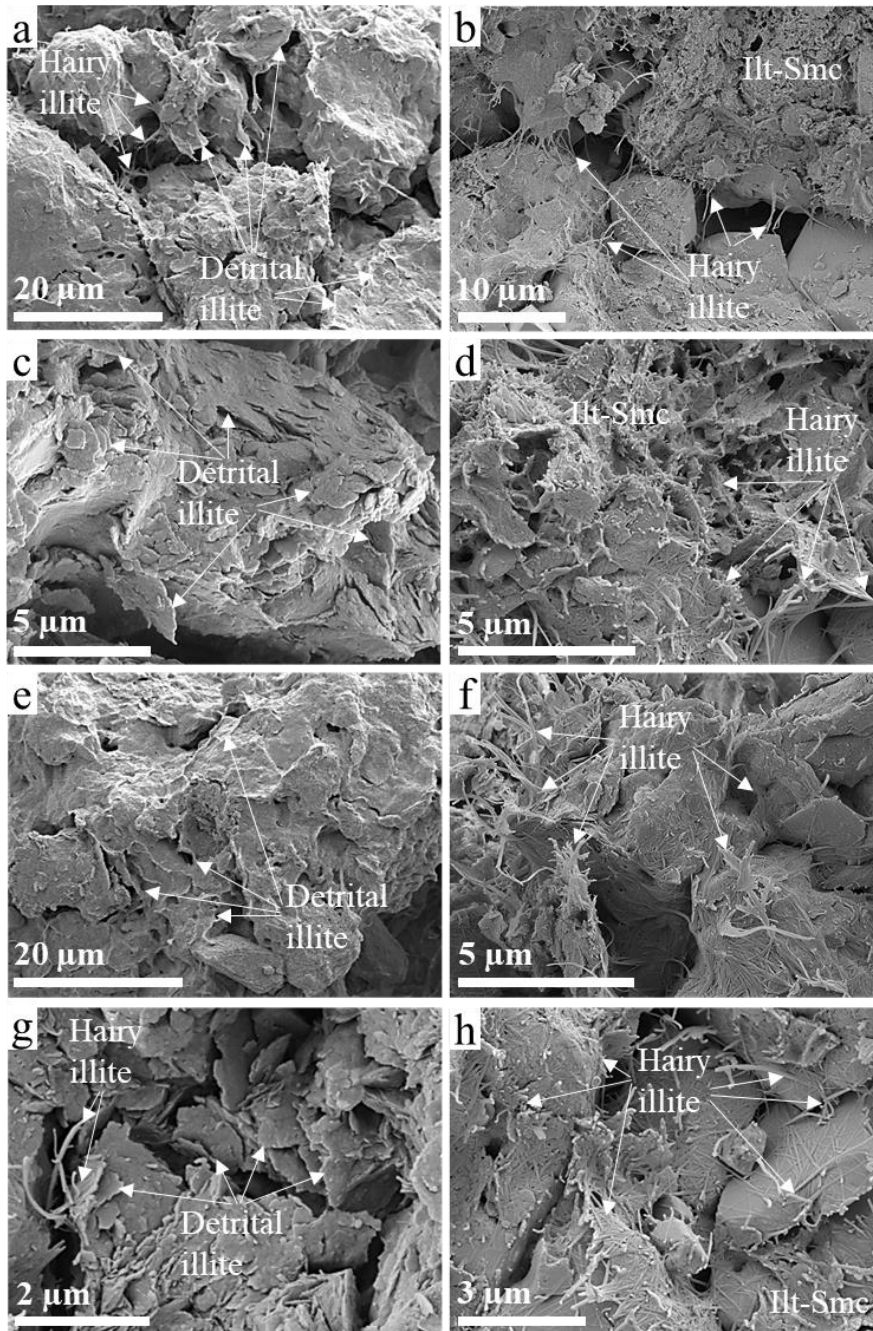
963

964 **Figure 2:** (a) Integrated lithostratigraphic profile of the investigated sedimentary succession
 965 from the Taatsiin Gol region, Valley of Lakes (modified after Richoz et al., 2017), with
 966 biozonation (modified after Harzhauser et al., 2017). (b-d) Field impressions of the sections
 967 Hotuliin Teeg (HTE) with calichized basalt II group, Tatal Gol (TAT-E) sediments and Taatsiin
 968 Gol right (TGR-B) section with basalt I group (modified after Daxner-Höck et al., 2017).



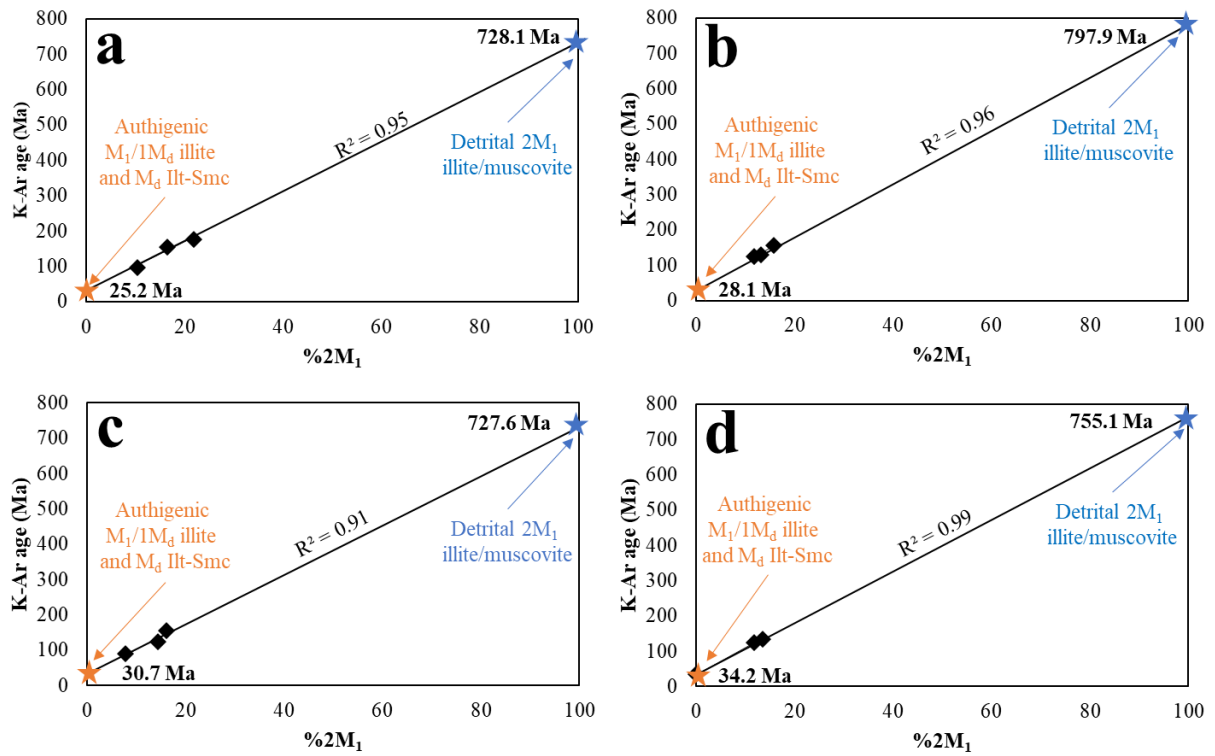
969

970 **Figure 3:** Averaged mineralogical composition (in wt%) of the sediments from the (a) upper
 971 Eocene Tsagaan Ovoo Formation, (b) Oligocene Hsanda Gol Formation and (c) lower Miocene
 972 Loh Formation from the Valley of Lakes, determined by XRD analysis.



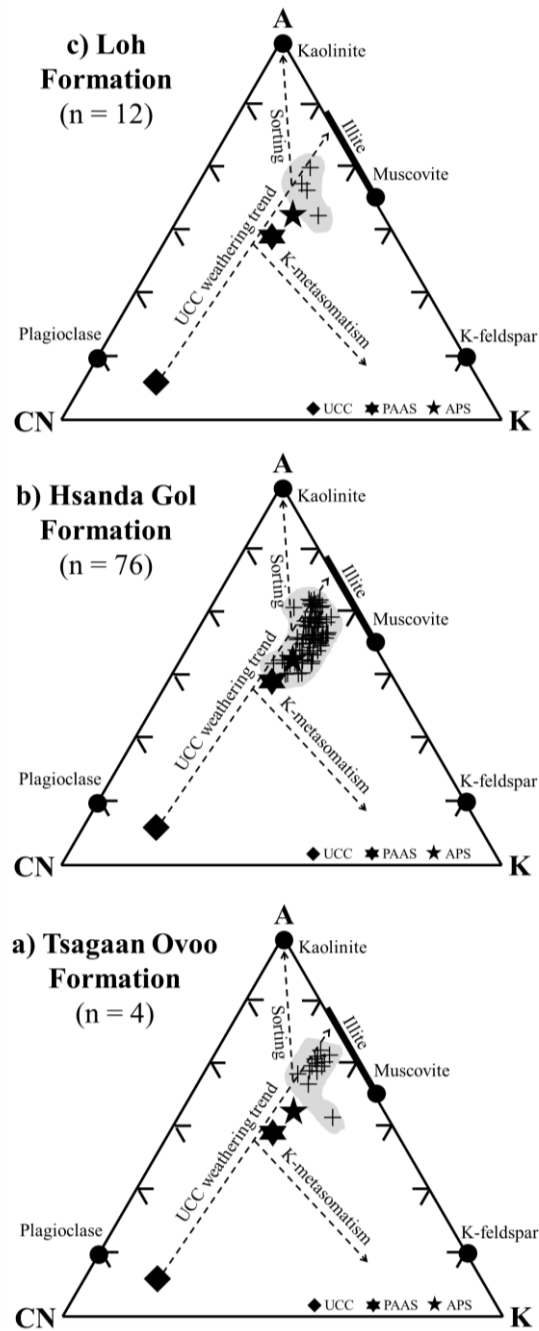
973

974 **Figure 4:** Secondary electron images of partly calichized and illitized silty to sandy deposits
 975 from the of the Oligocene Hsanda Gol Formation, Valley of Lakes, collected from (a-b) TAT
 976 section (~90.5 m), (c-d) TGR-C section (~78.0 m), (e-f) SHG-D section (~55.5 m) and (g-h)
 977 TGR-AB section (~35.0 m). The detrital illite/muscovite (left panel) occurs as coarse, rounded
 978 or pseudo-hexagonal platelets, whereas authigenic illite-smectite (Ill-Smc) and hairy illite (right
 979 panel) appear either as fine, flaky to irregular particles or as long, but thin laths and fibers, both
 980 covering detrital grains or growing into the open pores.



981

982 **Figure 5:** Crystallization ages of detrital $2M_1$ illite/muscovite and of authigenic $1M_d/1M$ illite
 983 and illite-smectite (Ilt-Smc) from the Valley of Lakes, calculated for sediments collected from
 984 (a) TAT section (~90.5 m), (b) TGR-C section (~78.0 m), (c) SHG-D section (~55.5 m) and
 985 (d) TGR-AB section (~35.0 m) using illite polytype quantification and K-Ar age systematics
 986 of different grain size sub-fractions (from left to right: $< 1 \mu\text{m}$, $1-2 \mu\text{m}$ and $2-10 \mu\text{m}$).



987

988 **Figure 6:** Al₂O₃-(CaO*+Na₂O)-K₂O (A-CN-K) ternary diagram of Nesbitt and Young (1984)

989 showing the compositional ranges of sediments from the Valley of Lakes, from the bottom to

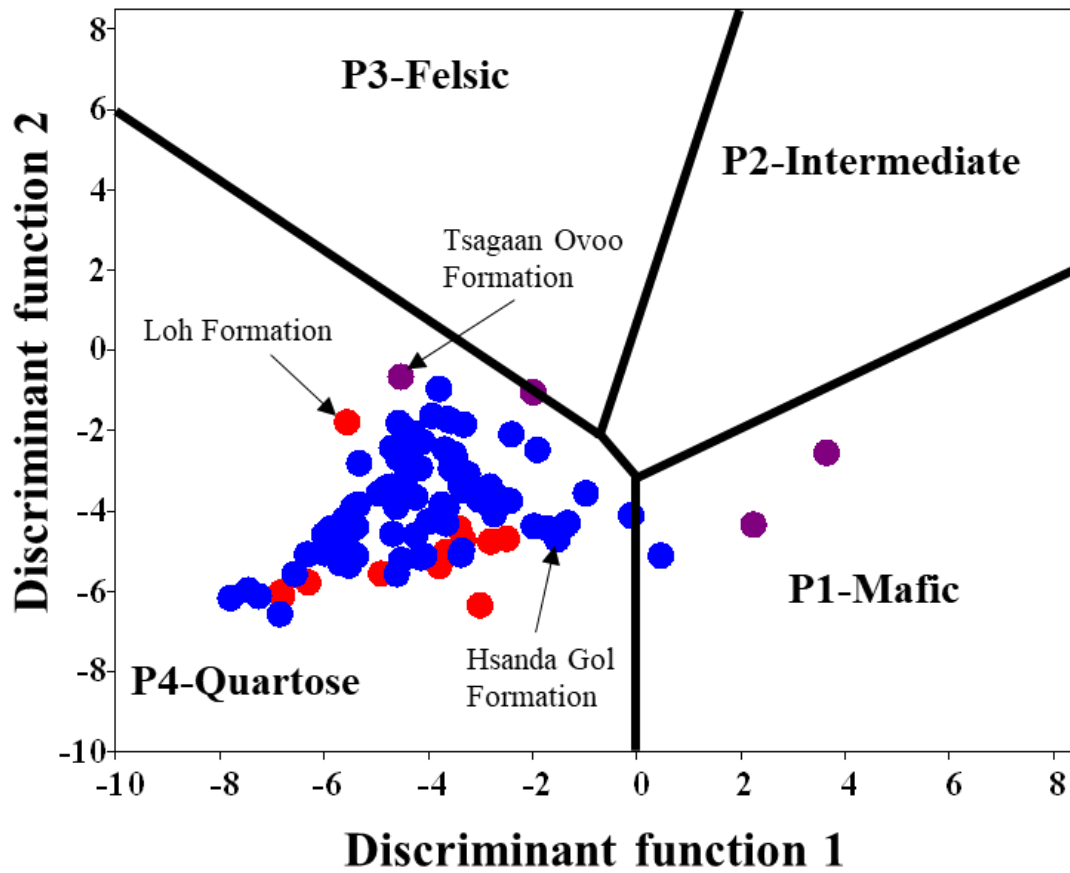
990 the top, from (a) upper Eocene Tsagaan Ovoo Formation, (b) Oligocene Hsanda Gol Formation

991 and (c) lower Miocene Loh Formation. Note that most samples are shifted to the K pole of the

992 diagram, which indicates a post-depositional enrichment of K₂O due to illitization. The

993 composition of Upper Continental Crust (UCC), Average Proterozoic Shale (APS) and Post-

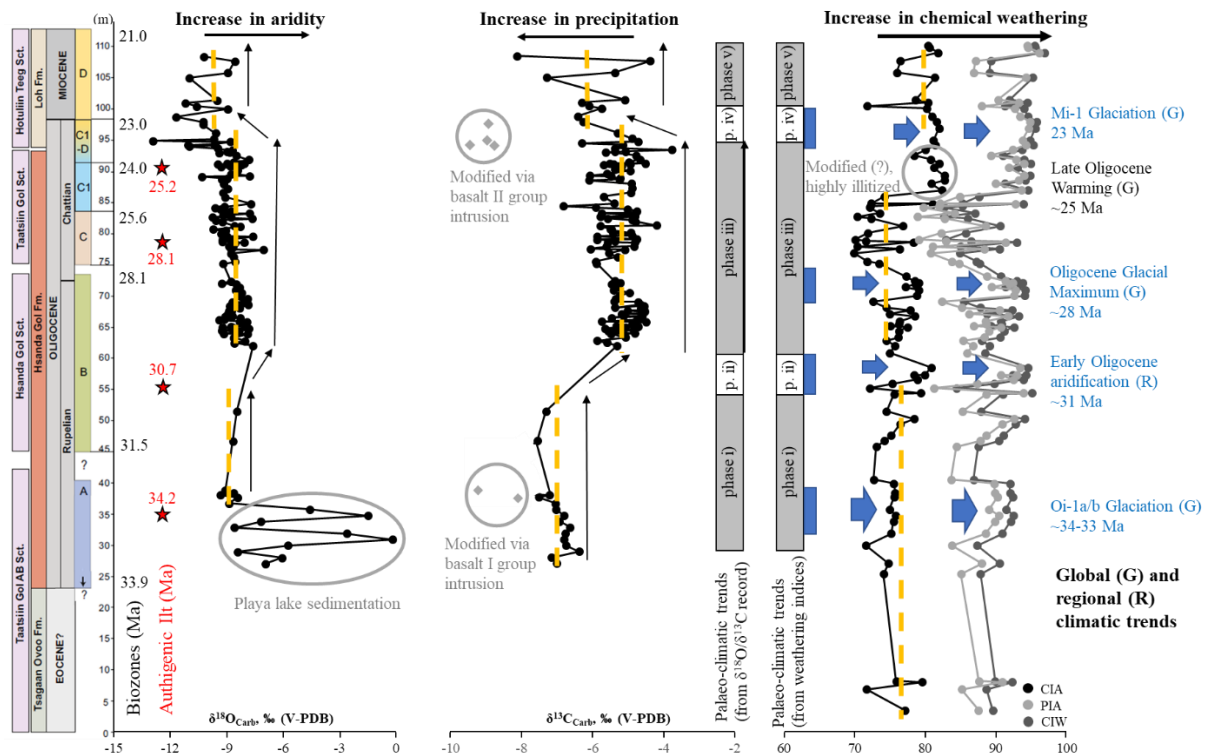
994 Archean Australian Shale (PAAS) are included for comparison.



995

996 **Figure 7:** Discrimination plot of discriminant function 1 and 2 indicating a narrow provenance

997 range (mainly type P4-quartzose) for the sediments from the Valley of Lakes, Mongolia.



998

999 **Figure 8:** Lithostratigraphic framework of the sediments from the Valley of Lakes (Mongolia,
 1000 Central Asia) showing the biozonation (modified after Harzhauser et al., 2017) and formation
 1001 ages of authigenic illitic (Ilt) phases obtained in this study (red asterisks), as well as soil
 1002 carbonate $\delta^{18}\text{O}$ and $\delta^{13}\text{C}$ isotope profiles and shifts in the silicate mineral-derived chemical
 1003 weathering indicators. Note that these hydroclimate proxies are inversely correlated and follow
 1004 long-term trends (indicated by orange dashed lines) in aridification or gain of humidity in this
 1005 region (indicated by black arrows). Increased chemical weathering degrees (highlighted with
 1006 blue bars and blue arrows) coincide with glaciation events documented in time-equivalent
 1007 marine deep-sea deposits (Zachos et al., 2001; Gallagher et al., 2020). Samples and intervals
 1008 outlined with grey circles are most likely modified due to the flows of the basalt I and II groups
 1009 or local strong illitization, and are therefore excluded from the palaeo-climatic interpretation.